

Probing Buried Interfaces within Organic Diodes  
Using Electromodulated Transmittance Spectroscopies

Bradley A. MacLeod

A dissertation  
submitted in partial fulfillment of the  
requirements for the degree of

Doctor of Philosophy

University of Washington  
2012

Reading Committee:  
David S. Ginger, Chair  
Charles T. Campbell  
Stefan Stoll

Program Authorized to Offer Degree:  
Department of Chemistry

University of Washington

**Abstract**

Probing Buried Interfaces within Organic Diodes  
Using Electromodulated Transmittance Spectroscopies

Bradley A. MacLeod

Chair of the Supervisory Committee:  
Professor David S. Ginger  
Department of Chemistry

We used two electrically-modulated transmittance spectroscopies on various device structures to gain better understand the physics built into interfaces within organic diode structures. In one line of investigation we noninvasively probed the buried interface between the transparent indium tin oxide (ITO) electrode and the polymer in functional, solution-coated organic polymer diodes. We systematically modified ITO electrode substrates with various dipolar phosphonic acids that form self-assembling monolayers (SAMs) to yield various effective work functions. We used electroabsorption spectroscopy to measure corresponding changes to the built-in potential across the polymer layer, which indirectly gives information about the ITO/SAM/polymer interface. This indirect probe revealed an interface that greatly deviates from typical observations of ambient-processed electrode-organic interfaces, appearing to behave more like “clean” electrode-organic interfaces that typically require ultra-high vacuum process conditions. In the second line of investigation we

use charge modulation spectroscopy (CMS) to look at charge transfer to-and-from plasmonic Ag nanoprisms (AgNPs). The AgNPs were previously shown to increase absorption within bulk heterojunction semiconductor blends used in organic photovoltaics (OPVs), but a spectroscopic fingerprint indicated that some portion of photogenerated free charges were transferring to the AgNPs. Using CMS, we verified that AgNPs which were not electrically insulated from the organic photoactive layer materials were being chemically reduced, posing a potential recombination pathway in OPV devices which would incorporate the nanoparticles. The two electromodulated spectroscopies probed buried interfaces within functional devices and device-relevant structures, both indirectly and directly, which stands out from many surface science techniques which either require exposed interfaces or which may alter the chemical composition upon probing. We gained previously unseen insight into two materials systems which can be used to improve the power conversion efficiency in organic photovoltaics.

# TABLE OF CONTENTS

LIST OF FIGURES .....	iii
LIST OF TABLES .....	v
PREFACE .....	vi
ACKNOWLEDGEMENTS .....	vii
DEDICATION .....	viii
CHAPTER 1 : Organic diodes and electromodulated transmittance spectroscopies .....	1
1-1. Introduction.....	1
1-2. A brief history of organic polymer photovoltaics.....	3
1-2-1. The single layer organic diode.....	3
1-2-2. The heterojunction.....	3
1-2-3. The bulk-blended heterojunction.....	5
1-2-4. Beyond the (simple) bulk-blended heterojunction .....	5
1-3. Thesis statement.....	8
CHAPTER 2 : Electroabsorption spectroscopy and electrode-polymer interfaces .....	9
2-1. Introduction.....	9
2-2. Sample preparation .....	13
2-3. Measuring work functions with LIXPS .....	17
2-4. EAS – Theory .....	21
2-5. EAS – Practical Application .....	27

2-6. Results and discussion .....	34
CHAPTER 3 : Charge modulation spectroscopy plasmonic nanoparticles .....	41
3-1. Introduction.....	41
3-2. Sample preparation .....	43
3-3. Results and discussion .....	44
CHAPTER 4 : Conclusions and future directions .....	51
4-1. Achievements.....	51
4-2. Suggested directions for EAS and PA SAMs .....	53
APPENDIX A : Appendix to CHAPTER 2.....	55
A-1. Equipment photos .....	55
A-2. Diode conditioning.....	57
A-3. Phosphonic acids from the Marder group.....	59
A-4. $V_{bi}$ in other polymer systems.....	59
A-5. UPS HOMO level for Super Yellow .....	66
A-6. Post-treatment of PA SAMs with a basic solution.....	69
A-7. LIXPS beam damage studies .....	70
A-8. XPS survey scans .....	72
A-9. Plasma cleaner-induced contamination identified with XPS.....	75
A-10. Vacuum-Referenced Energy Levels.....	77
BIBLIOGRAPHY.....	78

## LIST OF FIGURES

Figure Number	Page
Figure 2-1: Theoretical energy-level diagram of a simple diode.....	10
Figure 2-2: AFM Topography of ITO. ....	14
Figure 2-3: Phosphonic acids from the Marder group. ....	15
Figure 2-4: Organic diode and SY polymer structures. ....	17
Figure 2-5: LIXPS – Beam damage.....	19
Figure 2-6: LIXPS – Low kinetic energy feature for PA SAMs on ITO.....	21
Figure 2-7: Schematic of the EAS experiment. ....	27
Figure 2-8: Electroabsorption spectrum of ITO/SY/LiF/Al device.....	32
Figure 2-9: Electroabsorption voltage-scan of ITO/SY/LiF/Al device .....	33
Figure 2-10: Dark JC curves for of ITO/SAM/SY/LiF/Al devices. ....	35
Figure 2-11: $V_{bi}$ vs. $\Phi$ for ITO/SAM/SY/LiF/Al devices . ....	36
Figure 3-1: PIA spectra of P3HT:[60]PCBM and AgNPs.....	43
Figure 3-2: Schematic of the CMS experiment. ....	44
Figure 3-3: CMS of AgNPs .....	46
Figure 3-4: CMS of AgNPs – control structures. ....	49
Figure 3-5: CMS of AgNPs – different colored AgNPs.....	50
Figure A-1: Photos of the vacuum annealing chamber.....	55
Figure A-2: Photos of the experimental apparatus. ....	56
Figure A-3: Diode conditioning.....	57
Figure A-4: (a) poly(3-hexylthiophene) (P3HT) and (b) polyfluorene (PFO) .....	60
Figure A-5: EAS of ITO/P3HT/Al devices .....	62
Figure A-6: EAS of ITO/PPFO/Al devices .....	63

Figure A-7: $V_{bi}$ vs. $\Phi$ for PFO, SY, and P3HT devices. ....	65
Figure A-8: UPS and energy band diagram for ITO and ITO/SY.....	67
Figure A-9: UPS and energy band diagram for ITO/SAM and ITO/SAM/SY. ....	68
Figure A-10: LIXPS – More beam damage.....	70
Figure A-11: XPS – In $3p_{3/2}$ and F 1s. ....	73
Figure A-12: XPS – C 1s. ....	74
Figure A-13: XPS – O 1s.....	74
Figure A-14: Plasma cleaner O-ring contamination study. ....	76
Figure A-15: Energy levels of materials in the device studies .....	77

## LIST OF TABLES

Table Number	Page
Table 2-1: LIXPS $\Phi$ 's of PA SAMs on ITO.....	20
Table A-1: LIXPS binding energies at the low kinetic energy edge .....	71

## PREFACE

In some instances it may be beneficial to reference the location of the original data that a particular figure was derived from; in these instances the caption will read “Data located in group data storage at” followed by the relative file path location in the Ginger group network-attached storage. The file structuring naming convention was derived to be referenced to a specific location in the physical logbook. For example, the sub-directory named “BM8\_083\_x154 - PA SAMs XPS & EAS” refers to an experiment in **Bradley MacLeod’s** logbook **#8**, starting on page **#83**, being the **154<sup>th</sup>** enumerated experiment, relating to **Phosphonic Acid Self-Assembled Monolayers** being studies by **XPS** and **EAS**. In other instances, the logbook and page number may be referred to.

When describing the architecture of a thin film device within the text, the use of a slash “/” denotes the separation of two layers of different materials. In some cases these are nominally planar, but in all cases, it can be taken as the interface that is formed between subsequent layers of the structure that are produced layer-by-layer. In similar context, the use of a semicolon “:” designates two materials that form a composite layer.

## ACKNOWLEDGEMENTS

Foremost, I would like to acknowledge the success and hard work of my mother. Mom brought me up as a single parent and was able to provide the best of opportunities for me. She has always given me a great deal of support, no matter what I've been working on, and as I've moved around in the globe, she has provided me with the home to come back to, even when I wasn't able to hop on a plane. Thanks, Mom! Mom and I didn't go-it-alone and we share our successes with my sister, stepfather, grandmother, two uncles, and all of their families.

After beginning studies in electrical engineering at the University of Alaska Anchorage, I became involved with the Alaska Native Science and Engineering Program (ANSEP). This program provided me with financial support, opportunities to mentor and learn from my peers, a sense of community, and vast source of cultural enrichment throughout my undergraduate studies. Additionally, ANSEP placed me in a few good internships, which would eventually owe to my finding a career path in the sciences. I moved to the University of Alaska Fairbanks to finish my degree, where I received a great deal of advice from Boris Bracio, my simulations professor. He was very sympathetic to issues of the family, and offered me the opportunity to perform undergraduate research in his lab. Eventually, Boris convinced me that the type of work I would like to be doing would require further credentials – the PhD. The generous financial support from Cook Inlet Region, Inc. also allowed for a greater deal academic focus during undergraduate studies.

Arriving at the University of Washington, I was first greeted by Charlie Campbell. Charlie has provided my with a great deal of advice, both professionally and scientifically, and he's an all-around great guy to know. David Ginger was willing to take me on as an inexperienced research assistant and to illustrate for me the methods for achieving scientific goals. It was in his quantum chemistry class that I learned how deeply I could push the realms of my own knowledge. David has been always willing to teach, to provide direction, and to let me know when an idea was good or bad. Within his research group, I am indebted to those who have taken the time to teach me: Obadiah Reid for AFM skills, Liam Pingree for further AFM skills and practical device lab skills, Kevin Noone for spectroscopy and who has also been a friend outside of the lab and Deanna Rodovsky for showing me wet chemistry and sharing stories over beers. The rest of the Ginger Lab has also been a great group of researchers to work with. The National Science Foundation provided me with a Graduate Research Fellowship, and the entire Chemistry Department has been very supportive.

Finally, I acknowledge the many friendships that in themselves made life in Seattle quite worthwhile; those that enjoy a cold brew after a long day of work in the Ginger Lab, our exceptionally-close starting class of graduate students, especially Sam Berweger and Kevin O'Malley, with whom I've shared a number of great times in and outside of shop, and my Washington Beer Lovers buddies: Jon and Jen Linton - cheers to you!

## **DEDICATION**

To my sister Veronica: When the winds of passion fill your sails, your creativity and wonderment can take you as far as you'll hold fast. You may have to watch the telltales, but be prepared for the unexpected gusts!

# **CHAPTER 1:**

## **Organic diodes and electromodulated transmittance spectroscopies**

### **1-1. Introduction**

Since the discovery of the semiconducting conjugated polymer, vast amounts of research have gone toward the development of solution-processable semiconducting materials that could allow for low-cost manufacturing of semiconductor devices. The manufacturing techniques which can print or coat these semiconducting inks are quite analogous to technologies used in modern printing of textual products such as the newspaper<sup>1</sup>, and it can easily be imagined to manufacture these semiconducting devices at large scales of area in small scales of time. The potential for a high rate of printed area for organic semiconductors is attractive to reducing the bottom line for a manufacturer of thin film organic electronics such as transistors, emissive devices (solid-state lighting and organic light-emitting diodes, OLEDs), and solar cells (organic photovoltaics, OPVs). Indeed, small emissive devices are available in consumer electronics from several manufacturers, and there are several companies developing production lines for OPVs. It is worth reemphasizing the impact of this scalability and especially for the case of OPVs, where the ultimate cost savings will likely be realized in large-area integrated electrical generation systems. Solution-processed photovoltaics promise to reduce the price of solar photovoltaic electricity generation by reducing materials and manufacturing<sup>1</sup> costs while enabling new flexible and building-integrated form factors that could also reduce balance of systems costs.

With the many perceived and real benefits of this technology, organic diodes still have many shortcomings, mainly, their current cost of production, poor operational lifetimes, and low efficiency. The future cost will most certainly be lower for all organic semiconductor devices, as the manufacturing techniques are still relatively young, and the volume of production is yet underdeveloped due to their historically low performance. All organic diodes suffer from degradation and failure at rates greatly exceeding more developed technologies; this is primarily due to the reactivity of the organic materials with oxygen and moisture, which is accelerated in the presence of heat and short-wavelength electromagnetic radiation (UV light).<sup>2,3</sup> There are some research groups which look at encapsulation to mitigate the degradation from these exposures.<sup>4</sup> Further, new device architectures have resulted in great increases to the operational lifetime. Perhaps the most active area of research in OPVs has been toward improving their photoelectric power conversion efficiency, typically being cited as the component of performance by which sizable industrial investments are most dependent (the 10% commercial-feasibility benchmark<sup>5</sup>). The overall motivation for this thesis work is toward the success of OPV technologies such that they may be competitive sources of electricity in an ever-developing world. And so, we focus on understanding the underlying physical processes which govern efficient photoconversion in OPVs and which may contribute to the stability of the end product, in order to guide the engineering of the devices structures as a whole.

## 1-2. A brief history of organic polymer photovoltaics

### 1-2-1. The single layer organic diode

It is useful to discuss the efficiency-limiting processes in the modern OPV within the context of its historical development. Many detailed accounts of this history are available in the literature,<sup>6,7</sup> but some important milestones in this evolution are provided here for context. Early organic photodiode structures were fabricated by depositing a thin film of photoconductive polymer from solution onto a semitransparent “positive” electrode and thermally evaporating a metallic “negative” electrode on top. Degenerately doped transparent conducting oxides (TCOs) were soon adopted for their fair conductivity and transparency in the optical spectrum, with tin-doped indium oxide (indium tin oxide, ITO) being soon adopted and still in common use for many OPV and OLED devices. However, these devices made quite inefficient OPVs because of their excitonic nature; due to the low dielectric constant of organics, the photoexcited electron was not fully screened the positively-charged remaining vacancy (hole) and the two charge carriers remained tightly bound under mutual coulombic attraction.

### 1-2-2. The heterojunction

In 1992, Sariciftci et al.<sup>8</sup> demonstrated photoinduced electron transfer from a thin film of poly[2-methoxy,5-(2'-ethylhexyloxy)-p-phenylene-vinylene] (or MEH-PPV) to an adjacent layer of the C<sub>60</sub> Buckminster fullerene. The fullerene provided a high electron affinity for rapid electron transfer from the polymer; this donor-acceptor heterojunction was a critical improvement in OPV device architecture and was much more efficient at generating free

charges than organic-electrode interfaces. But, the early heterojunction devices failed to efficiently extract the freed charge carriers, in part due to the poor mobility (the rate of carrier motion with respect to electric field intensity) of the semiconductor polymer. The fullerene was also quite conductive of electrons and derivatives of the Buckminster fullerene are currently used in most champion performance cells to date. Further incremental improvements on this bilayer heterojunction were made with different electron donor polymers and by the addition of hole transport layers, which increased the hole transport efficiency for more balanced transport of opposite carrier types. The use of the heavily doped poly(3,4-ethylenedioxythiophene):poly(styrenesulfonate) (or PEDT:PSS) remains quite common in many organic diode structures being researched, both for its conductive properties and its ability to form ohmic contact with p-type semiconductors (due to its large work function,  $\Phi$ ), despite having several drawbacks<sup>9,10</sup>. Pettersson et al.<sup>11</sup> further improved on the bilayer heterojunction by first modeling the optical field intensity in the device and by changing thicknesses of the layers such that the field was most intense near the heterojunction interface. They discovered that the exciton had a diffusion length less than 10 nm in either the donor (a polythiophene) or acceptor (a fullerene) materials. This meant that light absorbed further than 10 nm from the organic heterojunction, or from the organic-electrode interfaces, did not contribute to photocurrent yield in OPVs. Active layer thicknesses were optimized for collecting photocurrent (on the order of the 2× the exciton diffusion length) but not all of the light incident on the cell could be absorbed in such thin films – full extinction of incident radiation requires greater than 100 nm of material for most organics.

### 1-2-3. The bulk-blended heterojunction

The next step was a bulk heterojunction (BHJ) which would overcome the so-called exciton bottleneck by creating a large surface area of donor-acceptor heterojunction while allowing for films which could absorb all incident visible radiation. While there were several earlier demonstrations of the BHJ, it wasn't until Hummelen et al.<sup>12</sup> synthesized a more-soluble form of the fullerene, phenyl-C61-butyric acid methyl ester (or [60]PCBM), that devices could incorporate enough of this fullerene to optimize charge transfer in a PPV-based BHJ OPV. By 2001, Shaheen et al.<sup>13</sup> demonstrated a BHJ cell in which the morphology of a PPV:[60]PCBM matrix resulted in quantum efficiencies (conversion of absorbed photons into separated electrons/holes) approaching unity, and with a power conversion efficiency of 2.5 %. Morphology studies played a large role in OPV research in the 2000's with control methods coming from various process solvents, post deposition treatments (thermal and solvent-vapor annealing), and the use of new donor and acceptor materials. At the time of drafting this dissertation, Mitsubishi Chemical is reported to have demonstrated a spray-coated OPV which achieved 10.0 % power conversion efficiency.<sup>14</sup>

### 1-2-4. Beyond the (simple) bulk-blended heterojunction

The many progresses in OPV performance can in part be attributed to materials development, such as new organic chromophores. However, many of the improvements also came from improvement in the mating of the materials in the OPV device structure, both at organic heterojunctions and at organic-electrode interfaces. It was noted by Cates et al.<sup>15</sup> that bulk blends of poly(2-methoxy-5-(3',7'-dimethyloctyloxy)-p-phenylene vinylene) (MDMO-PPV) and [60]PCBM resulted in higher hole-mobility in the MDMO-PPV domains due to intercalation of [60]PCBM in the MDMO-PPV side chains, showing that the material properties of donor and acceptor BHJ domains can vary from those exhibited in a single-

semiconductor layer. It has also been observed that surface energy will affect the solid-state formation of solution processed semiconductor layers, and can result in a nonhomogeneous distribution in the donor and acceptor materials. Characterization of the nanoscale planar segregation<sup>16-19</sup> and the vertical segregation<sup>20-22</sup> have been correlated with bulk measurements of completed-device performance. A wide range of additional studies have also correlated morphology with almost every metric of efficiency, in studies ranging from the macro- to nanoscales. Nevertheless, the degree to which this morphology dominates the observed power conversion efficiency is not fully understood and is actively debated.

In recent times, regioregular poly(3-hexylthiophene) (P3HT) has been blended with [60]PCBM to generate a long-running class of champion BHJ devices; with a standard vertical assembly of ITO/PEDT:PSS/P3HT:[60]PCBM/LiF/Al. The various aspects of performance in this class of devices could be the subject of an entire dissertation(s), and due to the vast amounts of research on this structure (perhaps stemming from the success of Shaheen et al.'s work<sup>13</sup> with the analogous structure using MDMO-PPV), it proves to be a useful benchmark in characterization of performance and device physics. While a large portion of the success is certainly due to the marriage of P3HT and [60]PCBM, the high power conversion efficiencies achieved were still marred by poor device lifetimes. In addition to being processed inexpensively and having high efficiency, polymer-based solar cells must also remain stable in the environment in which they will be used,<sup>2</sup> such as in a solar array in the sunny desert or on a rooftop module in rainy Pacific-Northwestern American city. One common mode of degradation in these “traditional” BHJ architectures is due to the oxidative properties of the low  $\Phi$  electrodes and the photoactive polymer.<sup>2,23</sup> The precise mechanisms may depend on the polymer used in a given BHJ device, and encapsulation of the device while processing in an oxygen/moisture-free environment may mitigate these effects to some extent. However, device testing in the absence of oxygen and

moisture, either by encapsulation of the device, or by testing in inert/vacuum atmospheres is unable to fully prevent the short/moderate time scale degradation of these traditional BHJ device.<sup>2,3</sup> It has been shown that both low- $\Phi$  metal electrodes and PED:PSS layers pose a threat to the stability of these BHJ devices.<sup>24</sup>

One significant advancement in BHJ OPV stability was the introduction of an “inverted” architecture,<sup>25,26</sup> or one in which the function of electron- and hole-collecting electrodes were switched in the vertical assembly. This architecture provides a few distinct advantages over the “standard” architecture. First, the low- $\Phi$  electrode could now be buried and isolated from the air-side of an unencapsulated device, allowing for materials other than LiF/Al or other reactive materials that might otherwise be thermally deposited onto the organic photoactive layer(s). Second, because the top electrode layer would now preferentially be formed from a larger- $\Phi$ , less-reactive materials could be deposited onto the organics, such as coinage metals, doped oxides, or even solution-processed conductive materials.<sup>24</sup> These benefits proved invaluable as performance lifetimes increased by orders of magnitude, even for devices which were stored/tested in ambient conditions without encapsulation.<sup>27,28</sup> Further, the material which provides hole-collection for this top electrode could also provide electron-collection for the bottom electrode of an adjacent cell on the top of a tandem stack, or what is referred to as the recombination layer that allows for the addition of photovoltages from the two serially-connected cells.<sup>29</sup> These advancements in architecture highlight the importance of understanding the device physics of interfaces, as the numbers of interfaces seem to grow with the efficiency of the OPV structures.

### 1-3. Thesis statement

We used two electrically-modulated transmittance spectroscopies on various device structures to gain better understand the physics built into interfaces within organic diode structures. In Chapter 2, we describe a line of investigation in which we noninvasively probed the buried ITO-polymer interface in single layer diodes. We systematically modified ITO electrode substrates with various phosphonic acids (PAs) that form self-assembling monolayers (SAMs) to yield various effective  $\Phi$ 's, measured with low-intensity X-ray photoelectron spectroscopy (LIXPS, XPS). We used electroabsorption spectroscopy (EAS) to non-invasively measure corresponding changes to the built-in potential ( $V_{bi}$ ) across the polymer layer, which indirectly gives us information about the ITO/SAM/polymer interface. This indirect probe revealed an interface that greatly deviates from typical observations of ambient-processed electrode-organic interfaces, appearing to behave more like “clean” electrode-organic interfaces that typically require ultra-high vacuum (UHV) conditions. In Chapter 3, we describe a second line of investigation in which we use charge-modulated transmittance spectroscopy (charge modulation spectroscopy, CMS) to look at charge transfer to-and-from plasmonic metal nanoparticles. These nanoparticles have previously been investigated for their ability to increase absorption in nearby organic chromophores, and therefore may be a useful route to increase efficiency in OPV devices. Using CMS, we verified that nanoparticles which were not electrically insulated from the organic photoactive layer materials were being chemically reduced (electron charging), posing a potential recombination pathway (loss mechanism) for OPVs which would incorporate the nanoparticles. In Chapter 4, we highlight achievements and what was learned about buried interfaces in OPV-relevant device structures using the same custom-built apparatus, and suggest future directions to build on the current findings.

## CHAPTER 2: Electroabsorption spectroscopy and electrode-polymer interfaces

### 2-1. Introduction

The power conversion efficiency of a photovoltaic diode device is the ratio of the maximum electrical power ( $P_{max}$ ) it can produce to the power of incident light on the photoactive area ( $P_{solar}$ ). This value can be described by a few parameters that can be determined by current-voltage measurements:

$$\eta_{PCE} = \frac{P_{max}}{P_{solar}} = FF \frac{I_{sc}V_{oc}}{P_{solar}} \quad 2-1$$

where  $FF$  is the fill factor,  $I_{sc}$  is the short-circuit current, and  $V_{oc}$  is the voltage at open circuit. These definitions are defined at the most basic level of device characterization. Characteristically,  $FF$  describes how well the photovoltaic behaves as an ideal diode in terms of the maximum power point on the current-voltage characterization sweep; a fill factor of unity would be displayed as a rectangle in the power producing quadrant of the current-voltage measurement with corners located at the origin,  $I_{sc}$  and  $V_{oc}$ . Lower fill factor are usually indicative of loss mechanisms, of one type or another, dominating the photovoltaic conversion process.  $I_{sc}$  indicates the efficiency of charge collection, or the rate at which photogenerated charges are collected.  $V_{oc}$  indicates how much potential energy the charges have gained and delivered to the external circuit upon photoexcitation. Measuring improvements in these parameters is then a rapid way to gauge improvements in the performance of a photovoltaic device.

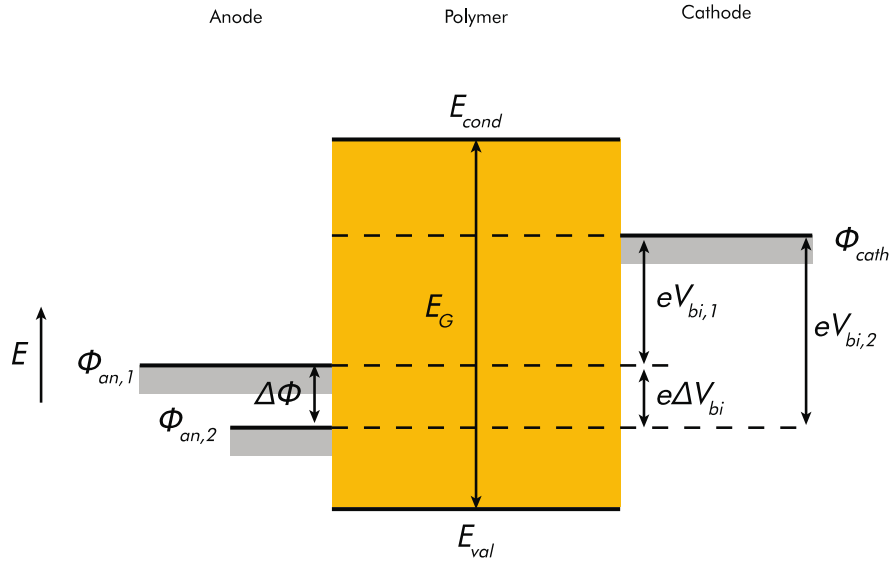


**Figure 2-1: Electron potential energy diagram for a single-layer polymer diode, in the Schottky-Mott limit, and at flat-band approximation. The valence and conduction bands of the polymer are shown, with the transport bandgap. In two otherwise similar devices, when the anode work function is changed by an amount  $\Delta\Phi$ , the built-in potential shifts by  $e\Delta V_{bi}$ .**

To the first approximation, the maximum  $V_{oc}$  that can be produced in a photovoltaic device is dictated by the potential energy difference of the photogenerated free electrons and holes; for BHJ OPVs, this is typically approximated by the LUMO of the electron acceptor and the HOMO of the electron donor, respectively. However, some degree of this potential energy is stored in the reorganization of bond structure to accommodate the presence of charge in a conjugate unit, and so the actual potential gap is dictated by the potential energy of the charge on a single-charged species, rather than the LUMO/HOMO of neutral species, and will therefore tend to be smaller. More accurately, the potential difference is then defined by the energy gap between the transport potentials of the two materials. The maximum photovoltage collected will be limited by the potential energies of the electrodes; charges will transfer to the lowest potential energy, and if the electrodes provide a lower potential energy, some photovoltage will be sacrificed at the electrodes. In the Schottky-Mott limit, or in metal-insulator-metal structures, there are no energy states available in the gap of the insulator for charges residing on electrodes to transfer to, and so

the adjacent layers of this type of device share a common vacuum level. If this limit is applied to an organic diode device (either a single layer device or a composite/BHJ active layer), the maximum potential energy that can be given collected from photogenerated free carriers would be limited to the potential difference of the electrodes, setting the ultimate upper limit this built-in potential

$$V_{bi} = (\Phi_{an} - \Phi_{cath})/e \quad 2-2$$

where  $\Phi_{an}$  and  $\Phi_{cath}$  are the work functions of the anode (hole collecting electrode) and cathode (electron collecting electrode), respectively, and  $e$  is the elementary charge. Figure 2-1 illustrates the relationship in Equation 2-2 and describes an experiment in which  $V_{bi}$  is measured in two theoretically constructed diodes that are otherwise identical, except for the work functions of the hole-collecting electrode (anode). Other factors may also contribute to the maximum  $V_{oc}$  such as the carrier density in the device which depends on operating conditions (illumination intensity, temperature) and semiconductor/device properties (mobility and built-in electric field); these conditions would necessarily violate the theoretically described device illustrated in Figure 2-1, shown for the aid to discussion. Therefore, one can imagine that for a BHJ device, the most desirable  $\Phi$  for the anode (cathode) is close to the hole (electron) conduction potential of the donor (acceptor) or hole-transport (electron-transport) layer, in order to maximize the upper limit on  $V_{oc}$ . If  $\Phi$  of an electrode material is outside of the semiconductor bandgap, the Fermi-level of the electrode and the charge transport level are said to be pinned. Because of Fermi-level pinning,  $V_{bi}$  (and  $V_{oc}$ ) cannot exceed the transport gap ( $E_G$  in Figure 2-1) of the active layer.

While there is currently some debate about the dominant loss mechanisms in specific OPV devices, several studies have indicated that field-dependent geminate recombination can play a role in many materials systems,<sup>30-39</sup> and many have argued that the collection of

photogenerated free charge carriers can depend on a drift field.<sup>40-42</sup> In these cases, understanding the electric field within the organic active layer is important in understanding the photocurrent generation and loss mechanism during device operation. More generally, measurements of the  $V_{bi}$  across the organic active layer can serve as an indirect probe of the electronic properties of the electrode/organic interface.<sup>43</sup> Several previous papers have measured  $V_{bi}$  in polymer diodes as the  $\Phi$  of the contacts was changed.<sup>42,44-47</sup> Additionally, ultraviolet photoelectron spectroscopy (UPS) has been used to measure barrier heights for charge injection in the organic, and in all cases where organic-on-metal interfaces are formed with at least one of the layers being processed in ambient conditions, Schottky-Mott behavior was observed.<sup>43</sup> On the other hand, deviations from this limit were observed for a large number of junctions between small molecule organics deposited on clean metal surfaces (both layers being formed in ultra-high vacuum without any ambient exposure).<sup>43</sup> This deviation was explained by the presence of a density of states, at the interface, within the organic layer. This deviation may be of relevance to OPV performance as it can affect the charge carrier concentration in the organic layers and at interfaces with electrodes.

The Marder group recently used a series of dipolar PAs to form SAMs on a TCO surface and demonstrated a shift in the oxide  $\Phi$  over a range greater than 1 eV.<sup>48</sup> These SAMs have also been shown to improve charge injection and electroluminescence performance in both small molecule<sup>49</sup> and polymer<sup>50</sup> LEDs. In this work, we utilized the PAs from the Marder group to prepare a series of functionalized ITO electrodes with  $\Phi$  spanning a similar magnitude, and we use EAS to probe the resulting changes in  $V_{bi}$ . There have been only two reports examining differences in  $V_{bi}$  for organic diodes where  $\Phi$  was varied by SAM-modification; both consisted of long, thiolated SAMs (non-conjugated<sup>51</sup> and  $\pi$ -conjugated<sup>44</sup>) on coinage metal surfaces and both displaying the Schottky-Mott behavior when  $\Phi$  was

within the polymer bandgap. For organic diodes using ITO modified by these PA SAMs, we find significant deviations from Schottky-Mott limit, which contrasts with what has typically been reported for organic-on-electrode interfaces in which an ambient process was used. In this chapter, we will describe how samples were fabricated, how  $\Phi$  was measured for functionalized surfaces, the theory of electroabsorption spectroscopy, how devices are characterized, and the analysis of the buried ITO/SAM/polymer interface.

## **2-2. Sample preparation**

Wafers of ITO on glass (Eagle XG, lot #071610) were purchased from Thin Film Devices, Inc. The ITO is specified by the supplier as being of  $145 \pm 10$  nm thick, total substrate thickness of  $0.7 \pm 0.1$  mm, and resistivity of  $20 \pm 2 \Omega/\square$ . The surface roughness was verified with an Asylum Research MFP3D atomic force microscopy (AFM) to be  $\cong 0.7$  nm (see Figure 2-2). A protective photoresist coating was applied to the wafers and they were diced in-house to  $15 \text{ mm} \times 15 \text{ mm}$  squares for use with diodes. Substrates were sonicated in acetone for 10 minutes to remove the protective coating and any large debris.

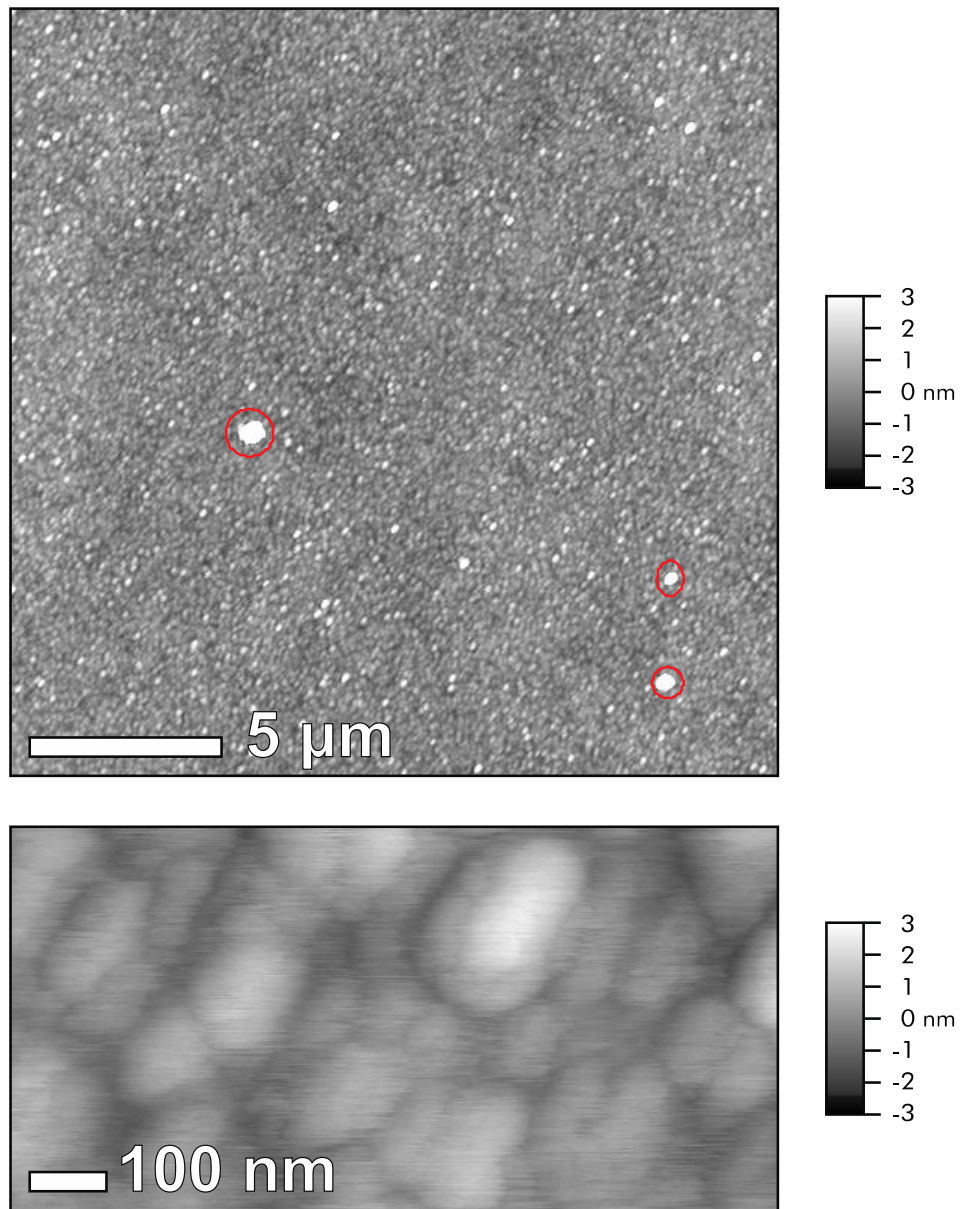


**Figure 2-2:** Asylum MFP3D atomic force microscope topography images of ITO surface, acquired in tapping-mode and post-processed in Igor Pro 6.2. (Top) 20 μm × 20 μm scan area, processed: 1<sup>st</sup>-order plane fitting in XY axes, 1<sup>st</sup>-order flattening, with circled features masked from the fit. (Bottom) 1 μm × 1 μm scan area, similarly processed. Data located in group data storage at \\Bradley MacLeod\Materials\TFD ITO\.

The substrates were then masked with Scotch Magic tape and etched with 25 mg/mL Zn in 1 M hydrochloric acid for 5 minutes to leave a 0.9 cm wide stripe of ITO, centered on the square glass substrate. After etching, the substrates were rinsed thoroughly with deionized water, and then scrubbed with isopropyl alcohol and a Kimwipes towel (or alternative) to remove any residual adhesive. The substrates were subsequently scrubbed with detergent solution (2 vol % Micro-90, International Products Corporation, in purified deionized water) using a toothbrush (or Kimwipes towel/alternative). Substrates were then sonicated in detergent solution, purified deionized water, and neat ethanol for 10 minutes each. To further clean the ITO and activate the surface for phosphonic acid SAM chemistry, the substrates were then oxygen plasma cleaned (Harrick Plasma HDC-32G on low, 6.8 W power setting) for 10 minutes; Appendix A-9 contains notes on the analysis of contamination during the plasma process. Plasma cleaner vacuum base pressure was < 10 mTorr from a rotary vane pump which is protected from oil backstreaming with a liquid nitrogen trap. The oxygen flow rate was set to 100 mL/min when leaked into the vacuum chamber.

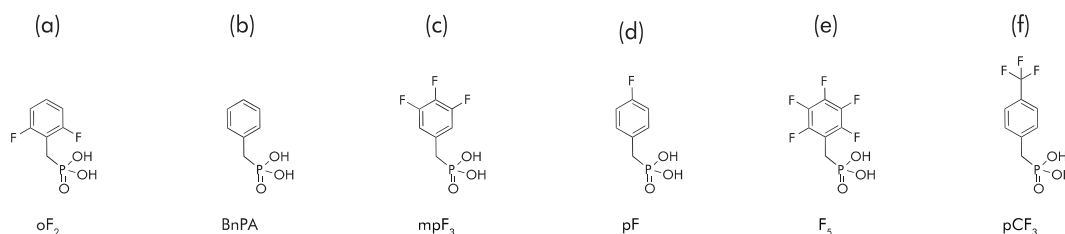


**Figure 2-3: Phosphonic acids from the Marder group used in ITO functionalization: (a) 2,6 difluorobenzylphosphonic acid, (b) benzylphosphonic acid, (c) 3,4,5 trifluorobenzylphosphonic acid, (d) 4 fluorobenzylphosphonic acid, (e) pentafluorobenzylphosphonic acid, and (f) 4 (trifluoromethyl)benzylphosphonic acid.**

The ITO was vented to atmosphere at approximately  $22 \pm 1$  °C and at 30-50% relative humidity and immediately submerged and sealed in a reaction vial at 75 °C. For the ITO control samples, the vial contained neat ethanol. The remaining reaction vials each contained

a 10 mM ethanolic solution of the phosphonic acid molecules shown in Figure 2-3 (supplied by Seth R. Marder and others at Georgia Institute of Technology, with syntheses being previously reported<sup>48,52</sup>). The substrates were incubated in reaction vials for 48 hours at 75 °C. Substrates were removed from incubation and rinsed in copious amounts of neat ethanol, such that no residuals or debris were visible, and then dried with a nitrogen gas blowgun. The substrates were further dried in a custom-built aluminum vacuum chamber (Figure A-1) at 140 °C using a similarly protected low-vacuum system. After vacuum-drying, the substrates were cooled and stored under static vacuum in this chamber. ITO and SAM-modified-ITO samples that were characterized with LIXPS (Section 2-3) were treated similarly up to this point with the exceptions that the initial substrates were smaller and were not etched. The XPS samples would be vented to atmosphere for mounting to the sample stage and immediately loaded into the XPS chamber, whereas the photodiode samples would be vented to a nitrogen glove box atmosphere (MBRAUN GmbH) containing < 5 PPM oxygen and < 0.1 PPM water for spincoating. Four or more hours prior to spincoating, the commercially available polymer known as Super Yellow (EMD Chemicals, PDY-132 - Figure 2-4, with structure proposed in the literature<sup>53,54</sup>) was dissolved (as-received) into neat anhydrous toluene at 6 mg/mL and the solution was allowed to stir on a hotplate at 65 °C to ensure full solvation of the solids, after which the temperature was reduced to 45 °C – overnight heating/stirring and agitation may be required in order to fully dissolve the polymer. Super Yellow solution was dispensed (100 µL) onto device samples initially at rest, with spincoating (Laurell Technologies Corporation, WS-400-6NPP/LITE) resulting in a film thickness of  $103 \pm 3$  nm (measured with Tencor Alpha-Step 500 Surface Profiler). The thickness was verified to be radially-uniform from the center to the edge of the substrate. Care was taken to mitigate non-uniformities that can arise from temperature gradients between spincoater, substrate, and solution (more problematic for spincoater models with

thermally-conductive chucks). Films were directly loaded into an integrated thermal evaporator (Angstrom Engineering Åmod 600 series) with a shadow mask to deposit 7 Å of lithium fluoride at 0.1 Å/s and pressure  $< 5 \times 10^{-7}$  Torr, defining 8 pixels each with an active area of approximately 4.2 mm<sup>2</sup>. The layer-by-layer composition of these diodes is illustrated in Figure 2-4. The chamber was vented to the glovebox atmosphere to exchange the lithium fluoride source with an aluminum source to minimizing cross-shadowing effects and 100 nm of aluminum was deposited at 1 Å/s and pressure  $< 5 \times 10^{-7}$  Torr. The devices were stored under static vacuum until use. For brevity, a “batch” of samples refers to a set of ITO substrates which share a reaction vial for a given phosphonic acid solution (or ethanol control) and are then vacuum dried in the same chamber; for a “batch” of photodiodes, the modified ITO would be spincoated from the same polymer solution onto each individual modified substrate and the LiF/Al contacts would be evaporated to all films simultaneously.

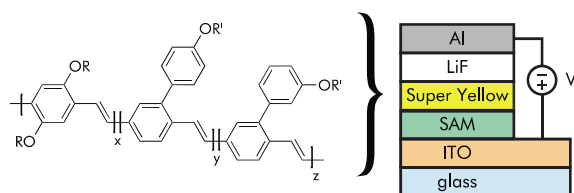


**Figure 2-4:** The proposed structure for the Super Yellow polymer repeat unit and the diode structure which incorporates it. Diode layers not to scale. External voltage supply shows the convention for biasing used in experiments.

### 2-3. Measuring work functions with LIXPS

The methods for determining the ITO and SAM-modified ITO substrate  $\Phi$ 's were informed by methods for LIXPS described in great detail elsewhere.<sup>55-58</sup> While UPS has been more widely used for the purpose of measuring surface  $\Phi$ 's, there was no locally-

available He UV source for performing such measurements. Further, LIXPS has been shown to be capable of measuring  $\Phi$  of ex-situ prepared oxide surfaces without altering the surface chemistry, unlike the typical flux of He and X-ray sources.<sup>55,59</sup> The PHI 5000 VersaProbe Scanning X-ray Microprobe system irradiates the samples with monochromatic Al K $\alpha$  photons (1486.6 eV) with source power set to “Idle” mode, analyzer pass energy of 2.95 eV, and at a pressure approximately  $2 \times 10^{-9}$  Torr. The energy analyzer calibration was verified according to the procedures in the VersaProbe Installation and Calibration Manual (Revision N) in which three freshly argon-sputtered metal foils (Alfa Aeser) were used; the energetic separation of the Au 4f<sub>7/2</sub> (83.96 eV) and Cu 2p<sub>3/2</sub> (932.62 eV) peaks was verified to be  $848.66 \pm 0.02$  eV by PHI Mulipak peak-fitting software and the hemispherical analyzer detector work function (and binding energy reference) was determined by referencing the location of the Ag 3d<sub>5/2</sub> peak (368.27 eV). We note that the peak assignment of Ag 3d<sub>5/2</sub> varies slightly to that designated by ISO 15472 (368.21 eV),<sup>60</sup> but is reproducible within the PHI specifications. The secondary electron cut-off (SEC) low kinetic energy feature was measured with the samples biased -15 V with respect to the detector (using a Keithley Model 2400 Series SourceMeter), and the SEC position was verified to shift in eV at unity proportionality with change in the applied voltage. The SEC step is nominally of infinite slope but due to detector and thermal broadening (not characterized here) has a finite width,<sup>61,62</sup> and so the energy location is taken as the first-derivative peak of intensity. The energy of the SEC was verified not to change over the number of scans required for statistical analysis and therefore is not believed to induce any change to the samples being measured (Figure 2-5).

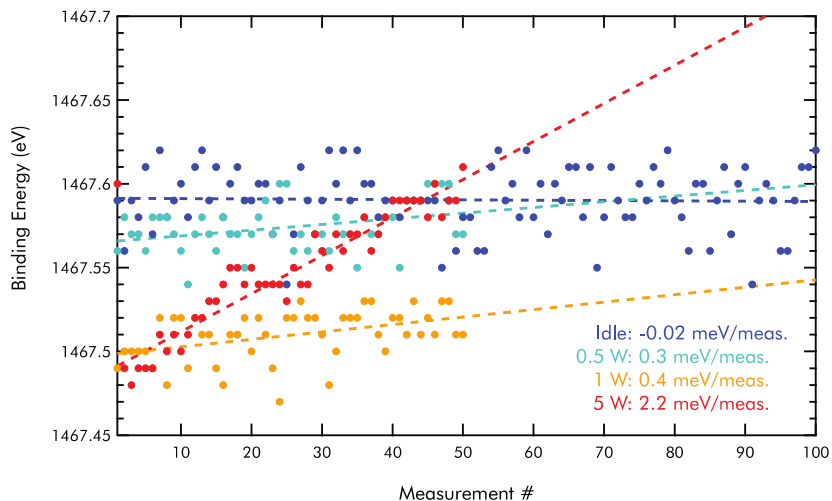


**Figure 2-5: Binding energy of the secondary-electron cut-off for subsequent measurements at the same spot on an ITO control substrate. Several X-ray power settings with lines showing a linear regression to the data are shown, and the measurement was performed from lowest to highest X-ray power. Data located in group data storage at \\Bradley MacLeod\BM7\BM7\_200\_x149 - XPS\XPS 2011-08-02\.**

The  $\Phi$  of the sample is then calculated by adding bias offset (-15 eV) to the source energy (1486.6 eV) and subtracting the measured SEC binding energy. In this section, we refer to a “sample” as an individual substrate on the XPS analysis stage, a “sample type” as being one of the PA SAMs (Figure 2-3) on ITO or the ITO control, and a “sample load” as being an event in which multiple *samples* of the same *sample type* plus the Au reference are all mounted/grounded to the XPS analysis stage and introduced to the XPS chamber from the laboratory atmosphere. The mean  $\Phi$ 's were determined from the measurement of 5 spots on each sample, with 2-5 samples per sample type, resulting in a mean values from 10-25 individual measurements per sample type. The Au reference was freshly Ar-sputtered at the beginning of every sample load. The resulting statistics of measurements performed on functionalized ITO surfaces are tabulated in Table 2-1, with original spectra shown in Figure 2-6. We observed that there was deviation in SECs between samples of the same type that was larger than deviation between spots on a given sample. And because we verified that the LIXPS method did not induce changes in the ITO control (Figure 2-5), we conclude that

these are actual differences in measured binding energies. Figure 2-6 shows the raw spectra that were used to tabulate the values in Table 2-1, with clustered traces of the same color indicating different spots on the same sample; for the Au traces, this was different spots in the same sample load. The source of this variation between samples is not known but three possible mechanisms are hypothesized: inhomogeneity in the sections of the original ITO wafer that each sample was taken from, small inconsistency in the photoelectron measurement geometry that could have resulted in changes of the energy or intensity of photoelectrons being detected,<sup>57</sup> or differences in the short time scale ambient-exposure (contamination) of the freshly plasma-cleaned ITO before submersion in the reaction vials. A freshly sputtered gold reference was measured with SEC binding energy yielding  $\Phi = 5.35 \pm 0.01$  eV (with standard deviation of the mean as error); which is in excellent agreement to what has been previously measured under similar circumstances,<sup>57</sup> but which varies from the commonly cited 5.1 eV taken from past editions of the CRC handbook. Subsequent sample SEC binding energies were then referenced to that of the same gold foil which was freshly sputtered and measured with each sample load as to account for any drift in the energy analyzer that may have occurred since the calibration procedure.

**Table 2-1:  $\Phi$ 's of the various PA SAM functionalized ITO surfaces as measured here with LIXPS (including one standard deviation of the mean for error) and elsewhere<sup>48</sup> using UPS.**

SAM Type	$\Phi_{\text{LIXPS}}$ (eV)	$\Phi_{\text{UPS}}$ (eV) <sup>48</sup>
<b>oF<sub>2</sub></b>	4.17 ± 0.01	4.3 ± 0.1
<b>(ITO)</b>	4.28 ± 0.02	4.5 ± 0.1
<b>BnPA</b>	4.45 ± 0.04	n/a
<b>mpF<sub>3</sub></b>	4.71 ± 0.03	5.3 ± 0.1
<b>pF</b>	4.96 ± 0.02	5.0 ± 0.1
<b>F<sub>5</sub></b>	5.14 ± 0.02	5.2 ± 0.1
<b>pCF<sub>3</sub></b>	5.30 ± 0.02	5.6 ± 0.1

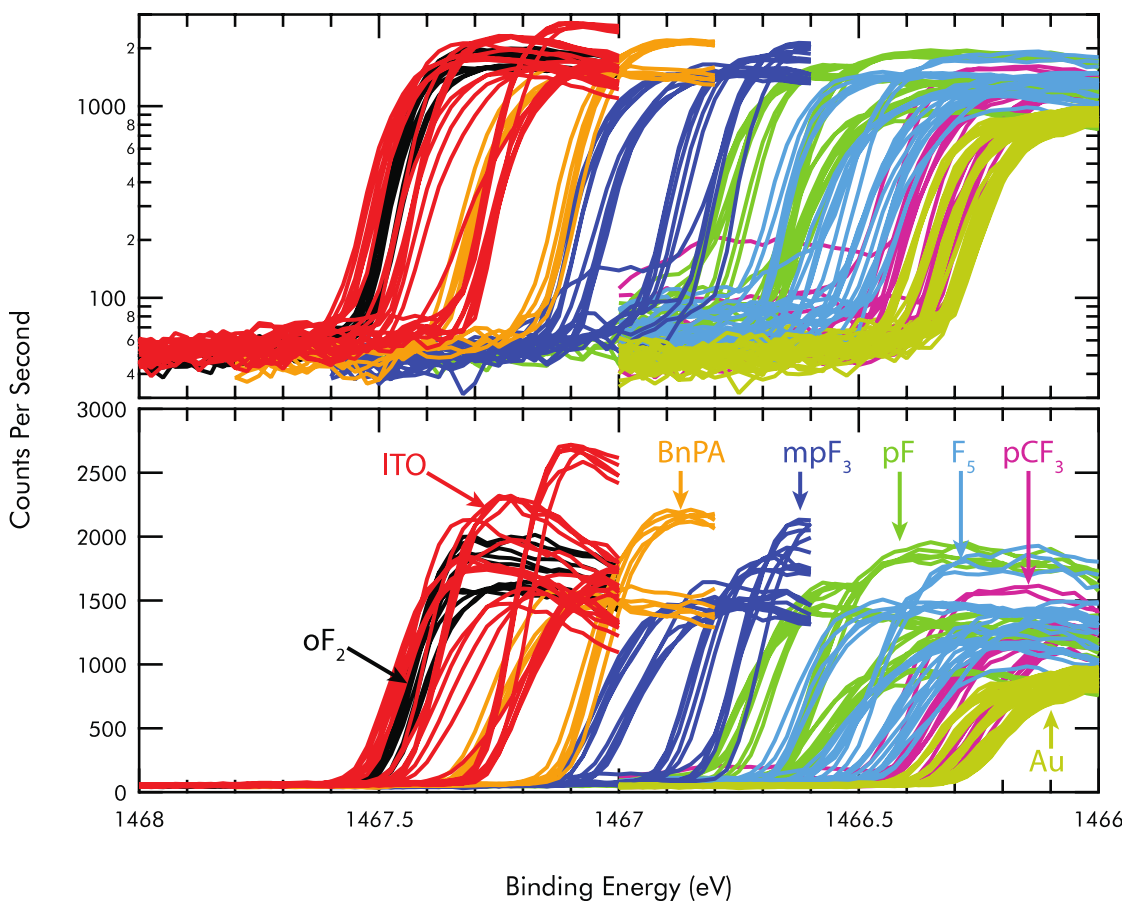


Figure 2-6: LIXPS spectra used to report statistical means and standard deviations in Table 2-1. (Top) Semi-log representation and (Bottom) linear representation with labels indicating the type of surface measured (ITO control, PA SAMs on ITO, and Au reference).

## 2-4. EAS – Theory

Simply stated, EAS is a technique in which a dielectric material is probed with a light source while under the influence of an externally applied electric field and light transmitted through the dielectric is detected. The field will induce changes in the absorption coefficient due to the so-called Stark effect (which may also be referred to as the DC Kerr effect and quadratic electro-optic effect). In a vertically-assembled organic diode device, the electric field is applied by means of a potential difference (bias) about the opposing electrodes

(biasing convention depicted in Figure 2-4). We probed the field-dependence of this Stark effect to reveal a potential-difference that is built-in to the organic diode by virtue of the electrodes having different chemical potentials (Figure 2-1, Equation 2-2). While EAS can be used to measure optical constants and other materials properties, the measurement of  $V_{bi}$  does not require as rigorous<sup>63-65</sup> a derivation of the field-dependent optical effects when certain experimental assumption can be made.<sup>51,66,67</sup> We will explain here the typical derivation<sup>68</sup> for the purpose of  $V_{bi}$  measurement, starting with a macroscopic description and progressing to the microscopic material properties.

The characteristic experimental response of EAS is given as

$$\frac{\Delta T}{T} = \frac{T(F) - T}{T} \cong -l\Delta\alpha(F) = -l(\alpha(F) - \alpha) \quad 2-3$$

where  $\Delta T$  is the change in transmittance to an applied electric field  $F$ ,  $T$  is the transmittance in the absence of the field,  $l$  is the path length of light (the polymer film thickness for normal incidence, or  $2\sqrt{2}$  times the thickness when at  $45^\circ$  from normal incidence), and  $\Delta\alpha$  is the change in absorption coefficient,  $\alpha$ , due to the field. This relation derives from the Beer-Lambert relation, with the approximate equality assuming that interference, multiple (internal) reflections, and reflectance at interfaces are negligible – transmitted light intensity is only a function of absorption in the polymer.

The field-dependent change in the absorption coefficient can be described from classical electrostatics. When an electric field impinges a dielectric, a displacement current  $D$  is induced which is proportional to the field intensity:

$$D = \varepsilon_0\varepsilon_r F = \varepsilon_0 F + \varepsilon_0\chi F \quad 2-4$$

where  $\varepsilon_0$  is the permittivity of vacuum,  $\varepsilon_r$  is the dielectric constant which is related to  $\chi$ , the susceptibility of the dielectric to an electric field. The second term of the displacement

current is known as the linear polarization of the dielectric,  $P = \epsilon_0 \chi F$ . In general, the susceptibility is expressed as field-dependent, and we obtain a nonlinear polarization when expanded as a power series:

$$P = \epsilon_0(\chi_1 F^0 + \chi_2 F^1 + \chi_3 F^2 + \dots)F \quad 2-5$$

The magnitude of nonlinear terms higher than  $\chi_3$  are negligible for the intensity of fields used here (the optical fields used here are relatively weak and do not contribute to nonlinear polarization) and the  $\chi_2$ -polarizability vanishes for systems that are isotropic or that have a center of symmetry (such as in conjugated polymers), so Equation 2-5 is simplified to

$$P = \epsilon_0(\chi_1 + \chi_3 F^2)F \quad 2-6$$

The dominant nonlinear polarization is due to the 3<sup>rd</sup> order susceptibility and carries an additional quadratic dependence on the field, which corresponds to a shift in the dielectric constant

$$\Delta\epsilon_r(F) = \epsilon_r(F) - \epsilon_r = \chi + \chi_3 F^2 - \chi = \chi_3 F^2 \quad 2-7$$

This field-dependent shift in the dielectric constant can then be used to describe the shift in the absorption coefficient by derivations, available in any introductory book on optics, which describe the attenuation of a propagating light wave in a dielectric

$$\Delta\alpha(F) = \frac{2\pi}{n\lambda} \text{Im}[\Delta\epsilon_r(F)] \quad 2-8$$

where  $n$  is the real part of the complex index of refraction, and  $\lambda$  is the wavelength of light. Substituting Equation 2-7 in to Equation 2-8, we see that the change in the absorption coefficient in a film of polymer, in the presence of an externally applied electric field, is proportional to the imaginary part of the 3<sup>rd</sup> order nonlinear susceptibility and is quadratic with the applied field

$$\Delta\alpha(F) = \frac{2\pi}{n\lambda} \text{Im}(\chi_3)F^2 \quad 2-9$$

Finally, when substituting Equation 2-9 into our characteristic approximate equality, we obtain the master experimental equation:

$$-\frac{\Delta T}{T} \cong \frac{4\pi\sqrt{2}d}{n\lambda} \text{Im}(\chi_3)F^2 \quad 2-10$$

which shows that the shift in absorption coefficient is measured in EAS as a fractional change in the transmitted probe light that is quadratic with the applied field, and is due to the field-dependent nonlinear susceptibility.

The shift in dipole transition energy that is due to the polarization of the material, and that is quadratic with the field can be derived with second order perturbation theory.<sup>64,69</sup> In a multilevel system where a majority of the oscillator strength is associated with transition from the ground state to the first excited state of the molecule (the optical exciton) the so-called quadratic Stark effect is given as

$$\Delta E^{(2)} = -\frac{1}{2}pF^2 \quad 2-11$$

where  $p$  is the molecular polarizability, or ratio of induced dipole moment to electric field intensity. Spectroscopically, the quadratic Stark effect shows a red-shift in the electroabsorption spectrum, with respect to the unperturbed absorption (as would be measured with the typical UV-Vis spectrophotometer). This is the primary contribution of the quadratic Stark effect to the overall observed change in transmittance when the energy shift is weak. However, if the energy shift is on the order of spacing between adjacent excited state energy levels, some degree of oscillator strength may be shifted to a forbidden transition, leading to excited-state Stark effect;<sup>70</sup> spectroscopically, this effect results in a change in the electroabsorption spectrum which is negatively proportional to the unperturbed spectrum, the exciton “bleach”.

The field also can act to shift the energy states by first order perturbation of the Hamiltonian,<sup>64,69</sup> resulting in the so-called linear Stark effect:

$$\Delta E_j^{(1)} = -\boldsymbol{\mu}_j \cdot \mathbf{F} \quad 2-12$$

where  $\boldsymbol{\mu}_j$  is the permanent dipole moment of a state  $j$ . Classically, this is analogous to permanent dipoles aligning in with an electric field. Conjugate units which have no permanent dipole moment or which are centrosymmetric, such as is common in polymers and other organic semiconductors, typically display no linear Stark effect. However, if the conjugate/chromophore unit is disordered, from defects or charge-transfer states, a non-zero contribution of the linear Stark effect may arise.<sup>70,71</sup> Any permanent dipoles will average-out when integrated over an isotropic distribution of orientations in the bulk, but a non-negligible electroabsorption may be observed from the McLaurin series (Taylor series about 0) expansion of  $\Delta\alpha$  with the energy shift.

$$\Delta\alpha(F) = \left\langle \frac{\partial\alpha}{\partial E} \Delta E \right\rangle + \frac{1}{2} \left\langle \frac{\partial^2\alpha}{\partial E^2} (\Delta E)^2 \right\rangle + \dots \quad 2-13$$

As stated, the first-order energy shift due to permanent dipoles will average out when integrated over all spatial orientations:

$$\left\langle \frac{\partial\alpha}{\partial E} \Delta E \right\rangle = \frac{1}{2} \int_0^\pi \frac{\partial\alpha}{\partial E} \mu_j F \cos\theta \sin\theta d\theta = 0 \quad 2-14$$

But the second order term does not:

$$\begin{aligned} \left\langle \frac{\partial^2 \alpha}{\partial E^2} (\Delta E)^2 \right\rangle &= \frac{1}{2} \int_0^\pi \frac{\partial^2 \alpha}{\partial E^2} \mu_j^2 F^2 \cos^2 \theta \sin \theta d\theta \\ &= \frac{1}{3} \frac{\partial^2 \alpha}{\partial E^2} \mu_j^2 F^2 \end{aligned} \quad 2-15$$

When Equations 2-11 and 2-12 are substituted into Equation 2-13, and truncated to quadratic field dependence, we obtain a more generic electroabsorption response that contains both linear and quadratic Stark effects:

$$\Delta\alpha(F) = -\frac{1}{2} \frac{\partial \alpha}{\partial E} p F^2 + \frac{1}{6} \frac{\partial^2 \alpha}{\partial E^2} \mu_j^2 F^2 \quad 2-16$$

This description allows us to obtain, at least, a characteristic description of the linear and quadratic Stark effect contributions to the electroabsorption response. For the purpose of measuring the  $V_{bi}$  in organic diode, we probe the field (bias) dependence in the spectral region where we expect to maximize quadratic Stark effect electroabsorption but minimize unperturbed absorption. We will show that the intensity of the electroabsorption can be kept relatively large below the peak of the unperturbed (UV-Vis) absorption, which should lead to minimal quadratic bleaching (excited-state coupling, quadratic Stark effect) as well as minimal photoexcited charge generation. The generation of charges in the semiconductor layer of the diode devices could possibly lead to the charge-transfer states or other disorder-inducing effects that result in generation of permanent dipoles.<sup>68</sup> Further free carriers that are present in the semiconductor layer will oscillate with the applied AC voltage, leading to charge-modulated absorption and bleaching, which for the purpose of measuring  $V_{bi}$  by electroabsorption is not ideal. Charge-modulated transmittance is however the technique that will be implemented in CHAPTER 2, for measuring the charging behavior in plasmon-resonant Ag nanoparticles.

## 2-5. EAS – Practical Application

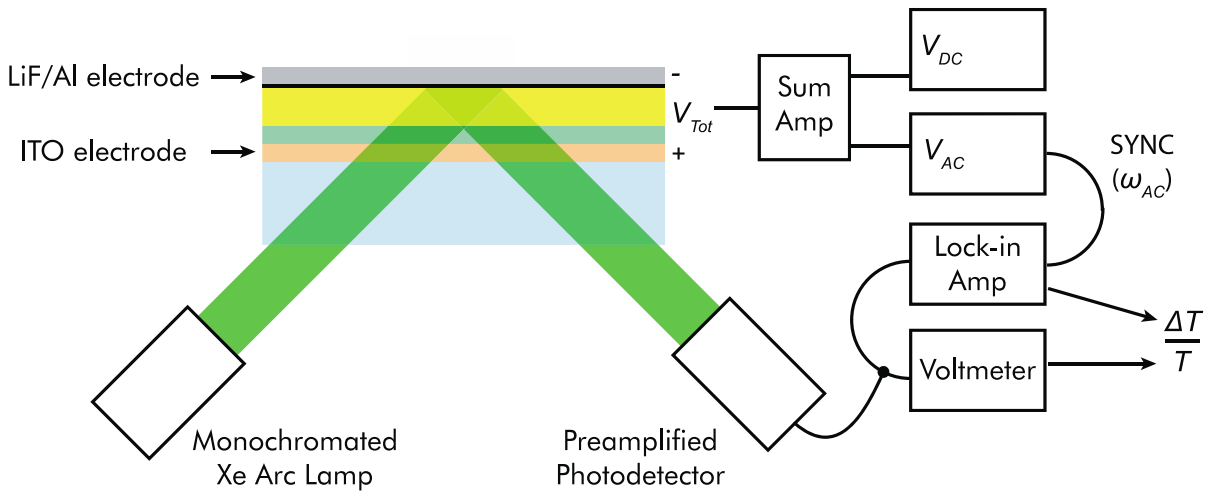


**Figure 2-7:** Schematic of the electroabsorption experiment showing a device under test of structure illustrated in Figure 2-4.

Figure 2-7 shows the schematic representation of the experimental apparatus. In the EAS experiment, the probe light shines on the organic diode device while the sum of an AC and DC bias ( $V_{AC}$  and  $V_{DC}$ ) is applied to the electrodes. The potential difference across the organic layer leads to the change in absorption described in the previous section, which results in  $\Delta T$  at the frequency of oscillation ( $\omega_{ac}$ ) of  $V_{AC}$ . The DC transmittance ( $T$ , equivalent to the unperturbed transmittance when normalized by the experimental system response) is recorded with a voltmeter (Keithley Model 2400 Series SourceMeter) and  $\Delta T$  is simultaneously recorded with a lock-in amplifier (Stanford Research SR830); both are preamplified (Stanford Research SR570). The output of the lock-in amplifier channels are scaled to convert from the RMS value to the peak value. The ratio of  $\Delta T/T$  gives the electroabsorption signal.

Recalling from Equation 2-9, the electroabsorption signal is proportional to the square of the total electric field within the polymer layer of the diode device. Assuming a uniform field distribution, the field within a polymer film of thickness  $d$  is given by the potential difference

across it:  $F = V/d$ . The total potential difference is given by the summation the AC and DC applied voltages and the built-in potential (which is opposing in sign under this biasing convention):

$$V = V_{ac} \sin \omega_{ac}t + V_{dc} - V_{bi} \quad 2-17$$

$$V^2 = \left[ \frac{1}{2} V_{ac}^2 + (V_{dc} - V_{bi})^2 \right] + [2V_{ac}(V_{dc} - V_{bi})] \sin(\omega_{ac}t) - \left[ \frac{1}{2} V_{ac}^2 \right] \cos(2\omega_{ac}t)$$

2-18

The quadratic expansion of the total potential difference shows that there is three terms: a DC term, an AC term at the fundamental frequency, and an AC term at the second harmonic of the modulation frequency. When the preamplified photovoltage signal is routed to the lock-in amplifier, and the lock-in amplifier is phase-referenced to the fundamental frequency of modulation for the function generator (AC voltage source), the lock-in amplifier filters out both the DC and second harmonic term. When the ratio of the AC to DC response is taken, the system response function is normalized, leaving the fractional change in transmittance signal:

$$\frac{\Delta T}{T} \propto (V_{bi} - V_{dc})V_{ac} \quad 2-19$$

This relation shows that the intensity of the signal can be experimentally scaled by adjusting the magnitude of the AC and DC voltages. Further, if the DC bias is equal in magnitude to  $V_{bi}$ , the  $\Delta T$  response vanishes. To the first approximation, the applied bias which nullifies the electroabsorption response indicates the magnitude of  $V_{bi}$ , but in practice there can be charge-modulated contributions to  $\Delta T$  that cause deviations from the otherwise linear response with  $V_{DC}$ . If the organic layer of the diode accumulates a significant density of free carriers, the charges will oscillate in response to  $V_{AC}$ . This effect can be minimized by operating the

experiment at conditions which minimize the presence of free, mobile carriers in the polymer layer. One simple approach is to perform EAS measurements at large negative biases; the large drift field in this polarity act to rapidly deplete the device of any free carriers that may be present. This of course cannot be implemented when attempting to null the response in Equation 2-19, but as will be shown, the linearity of this response in depletion conditions can be reliably extrapolated to the zero signal axis for determining  $V_{bi}$ . Further, we will probe the bias dependence of the  $\Delta T/T$  response at sub-bandgap wavelength such that no carriers are photogenerated.

To determine an appropriate wavelength for scanning the bias-dependence of the electroabsorption signal, the electroabsorption spectral response was recorded with a fixed bias, typically with a large AC voltage and largely-negative DC voltage. A 75 W Xe arc lamp (Osram Sylvania 69231) is focused with a parabolic mirror within the lamp housing (Newport/Oriel, Photomax 60100) into a monochromator (Acton Research Corporation, SpectraPro 2150i), which is equipped with order-sorting filters and utilizes a 500 nm blaze, 300 grooves/mm diffraction grating, and manually-operated slit width micrometers. If the device acts sufficiently as a photodetector, alignment with the optical focus of the probe beam can be done with the monochromator set to a wavelength above the band gap, and by adjusting the XY translator (located at the base of the assembly shown at bottom left of Figure A-2) for maximal photocurrent. For systems which do not produce a sufficient photocurrent response, this is primarily achieved by eye. One can attempt to maximize the reflected/transmitted light intensity as a secondary alignment-normalization process, but this does not ensure that the light being measured is transmitting through the active area of the device under test. The rule of thumb is that it is better to under-fill the pixel and over-fill the photodetector, if the focal image size cannot be matched exactly to the active area of the pixel and photodetector. The assembly shown at bottom left of Figure A-2 is not perfectly

rigid, and so translational adjustment should be done with attempts to normalize any hysteresis in the movement. The entrance and exit slit widths are then set to maximize the signal-to-noise of the electroabsorption signal while maintaining reasonable spectral resolution (assuming some earlier knowledge of the electroabsorption response for that particular system). These settings depend on the quality of the alignment of the parabolic reflector in the lamp housing and the general throughput of the optics (including the linear and nonlinear response of the device that is being probed), but typical slit widths are 100  $\mu\text{m}$  at both entrance and exit ports. This setting was calibrated with a spectrophotometer (Ocean Optics USB2000) and neutral density filtration to result in approximately 3.3 nm full-width half-maximum monochromation. Periodic replacement of the lamp requires the realignment of the parabolic reflector in the lamp housing; the parabolic mirror was adjusted to obtain maximum output from the monochromator at 530 nm with the appropriate order sorting filter in place. For rapid alignment and benchmarking of throughput, a Si photodetector (OSI Optoelectronics, PIN-10DP/SB) was placed directly against the output slits and the photocurrent was measured directly with the Keithley Model 2400. Typical power for these settings is on the order of 10  $\mu\text{W}$  at 530 nm. For the electroabsorption experiment, light exiting the monochromator is collected and focused with a 2-inch fused silica biconvex lens of 100 mm focal length. Light is focused onto a device pixel housed in a custom vacuum test chamber, shown in the bottom of Figure A-2. The chamber is pumped at typical low-vacuum pressure for a rotary vane pump ( $\leq 1$  mTorr). As depicted in Figure 2-7, light is incident on the vertically-assembled diode structure at  $45^\circ$  from glass-surface normal. Light is transmitted through the remaining layers of the device, being reflected off of the back electrode and transmitted out of the device testing chamber at  $90^\circ$  from incidence. Transmitted light is then collected with a 1-inch fused silica biconvex lens of 35 mm focal length and focused onto a Si photodetector (Thorlabs FDS1010) of relatively high bandwidth.

To optimal modulation frequency in our lab was found to be 4 kHz and was used for all electrically modulated measurements reported in this dissertation. This was determined by scanning the frequency spectrum of the function generator and taking several measurements at each frequency in the log-interval; the ratio of the mean to the standard deviation gives a reasonable indication of the signal-to-noise ratio. Also, the current preamplifier input stage capacitor was tuned for optimal frequency response for the Si photodetector. This was done by shining an LED on the photodetector that was driven with a square pulse train from the function generator. The output is monitored with an oscilloscope and the tuning capacitor of the preamplifier is adjusted for the sharpest reproduction of the pulse train.

All electronics are controlled with a personal computer running custom software that was written in the National Instruments LabVIEW 2010 environment. We note that aberrations in our optical probe system can lead to small fraction of probe light which does not focus in the primary focal plane, and is therefore lying outside of the device pixel active area that is under test. This unfocused light may still be collected by the photodetector, leading to a  $T$  (any collected light) which is disproportionately increased relative to  $\Delta T$  (only transmitted light which has passed through the active layer with an incident AC electric field). Care was taken to mitigate this effect and consequently, lower illumination intensities (thinner monochromator slit widths) typically gave the most accurate  $\Delta T/T$  spectra. The amplification ranges for the preamplifier and lock-in amplifier are set and held constant during the spectral scan, at the highest range which does not lead to saturation, in order to maintain an absolute phase relationship between in-phase and quadrature modulated responses. Non-zero quadrature intensity may then be used to identify response which is periodic but not due to the excitonic Stark effect, such as modulating charges in the semiconductor layer or the unmodulated reflectance already described. A drawback to the constant-phase method is that a lower signal-to-noise ratio is achieved for spectral regions where the DC transmittance is

low, and generally limits the range over which accurate spectral data can be accumulated in a given measurement, with the greatest degree of noise occurring at short wavelengths, where polymer absorption is strongest.

After spectral analysis, the wavelength for the voltage scan was chosen such that absorption (photogenerated carriers) was minimized but that signal-to-noise ratio was large (close to the sub-bandgap peak of the electroabsorption response). For the device response shown in Figure 2-8, the wavelength of 528 nm is sufficiently-far below the extinction peak of the polymer (red dots), while still contributing a significant intensity of the modulated in-phase response (blue-filled circles). Also shown in Figure 2-8 is the quadrature response (blue unfilled circles) which is for all intents negligible, but does show that at short wavelengths that the constant phase of detection and unperturbed extinction lead to lower relative  $\Delta T$  and  $T$  signals and hence, a higher degree of noise.

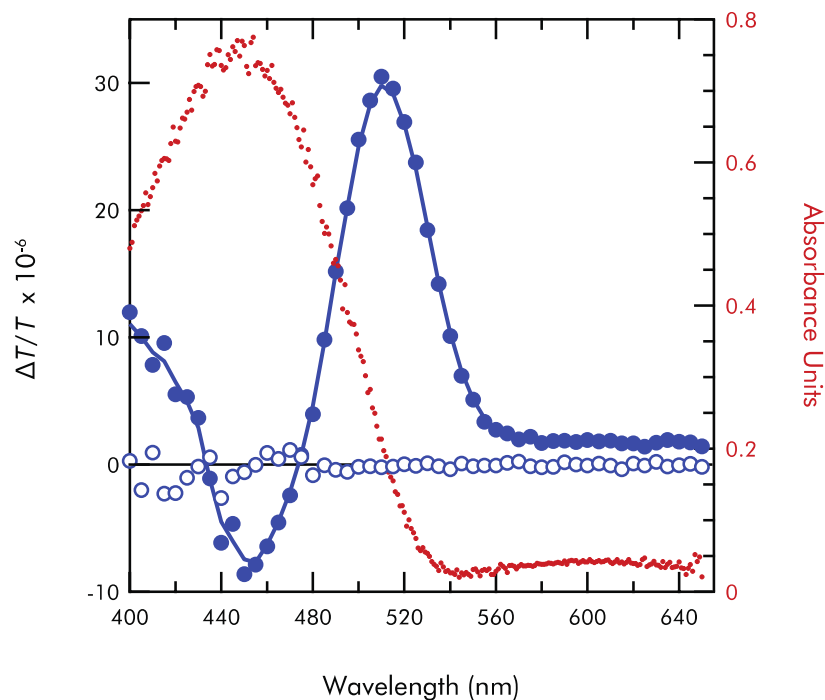


**Figure 2-8:** The absorbance of a 103 nm thick Super Yellow film is shown in the red dots on the scale of the right axis. The electroabsorption spectrum of a diode made from the same film, of structure shown in Figure 2-4 but without a PA SAM, is shown on the scale of the left axis. The blue-filled circles are the in-phase (X-channel) response, with line as a guide to the eye, and the blue unfilled circles are the negligible quadrature (Y-channel) response. These spectra were recorded at -5 V DC, 1 V AC (peak-to-peak), and modulation frequency of 4 kHz.

With the probe wavelength held constant, the DC bias is scanned at 1 V AC (peak-to-peak) to obtain  $V_{bi}$ . It was verified that the same  $V_{bi}$  was obtained with AC voltages as low as 0.2 V, but larger voltages significantly reduce the time required to achieve a comparable signal-to-noise ratio (Equation 2-19). Figure 2-9 shows the voltage-dependent response for the same device as in Figure 2-8. Generally, the electroabsorption signal intensity varies linearly with negative DC voltages, as is predicted by Equation 2-19, but can become non-linear close to zero-field conditions at positive-bias, which is attributed to charge-modulated effects. Further evidence to support this is in Appendix A-2, where the feature is seen to be connected with a current-induced conditioning of the diode that results in larger currents injected under forward bias. Due to the charge-modulated contribution, the  $V_{bi}$  of the charge-depleted device was defined by fitting a linear-regression to the negative bias regime of this voltage-scan, typically from -5 V to 0 V.

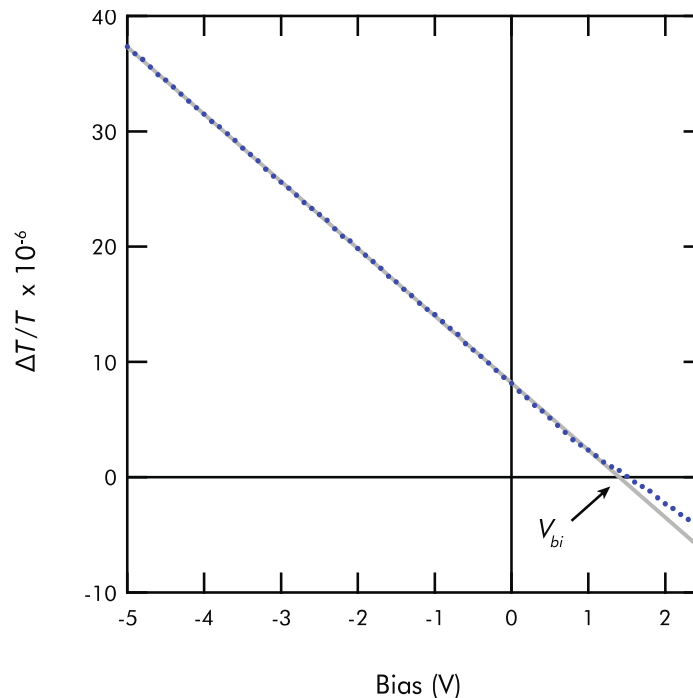


**Figure 2-9:** The bias-dependent electroabsorption response of the same device as in Figure 2-8 is shown in blue dots. The response is recorded at a constant wavelength of 528 nm and 1 V AC (peak-to-peak). The underlaid gray line is the linear fit to data point from -5 to 0 V DC, extended across the entire range of the plot.  $V_{bi}$  is defined by the intercept of this fit with the X-axis.

## 2-6. Results and discussion

Single layer SY polymer diodes, of the structure in Figure 2-4, were fabricated using the PA SAMs of Figure 2-3 (plus an ITO-only control) were fabricated using the methods outlined in Section 2-2. Conductive silver paint was applied to the Al contacts above the etched area of the underlying substrate (non-active area) to provide more reliable contact to the test pins. The device was transferred to the optical testing table (Figure A-2, top) sealed in the test chamber (Figure A-2, bottom right) under nitrogen atmosphere, where a low-vacuum system pumped on the sample during testing, such that the device was never exposed to atmospheric conditions. This vacuum state should act to slow any photooxidation or water-induced degradation effects.

External bias was applied to the common ITO contact with the reference potential applied to the silver-painted Al contact, as indicated in Figure 2-4 and Figure 2-7. For the devices in this study, a forward-bias current conditioning was implemented in which devices underwent an irreversible change leading to current-voltage characteristics which reproducibly displayed space-charge-limited current response (Appendix A-2). Current-voltage characteristics were recorded for each pixel with the device shielded from light. The devices were characterized first by measuring their current response as a function of applied bias, in the dark. Figure 2-10 shows the current density measurements in response to applied bias at room temperature. The current-voltage curves show that the four substrates with the largest  $\Phi$ 's give progressively larger currents under forward bias. The substrates with the smallest  $\Phi$ 's, benzylphosphonic acid (BnPA) on ITO, 2,6-difluorobenzylphosphonic acid (oF<sub>2</sub>) on ITO, and un-modified ITO, all exhibited smaller and similar injection-limited currents.

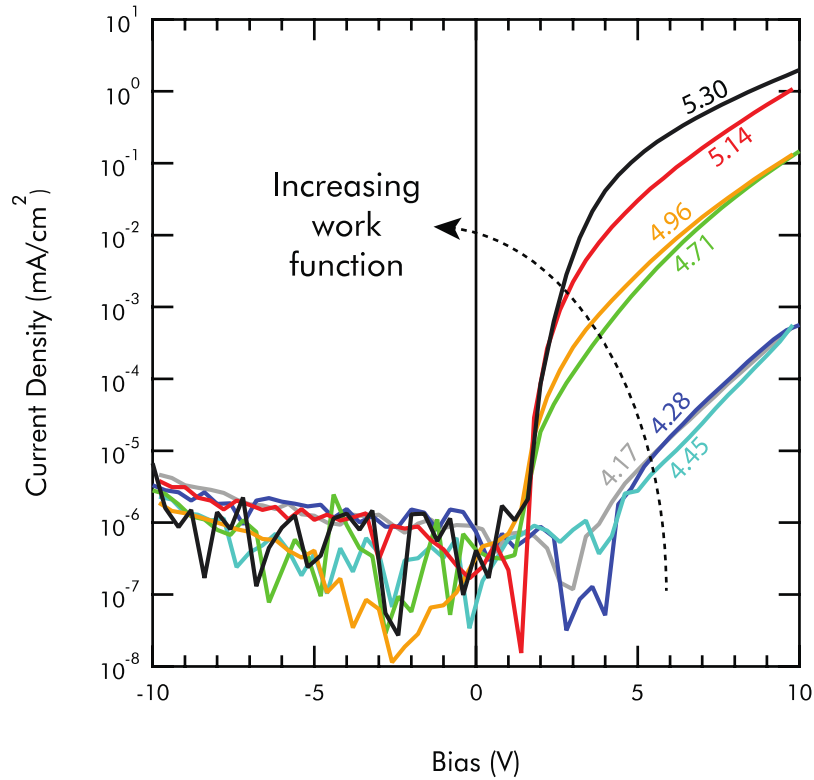


**Figure 2-10: Representative traces of the dark current-voltage measurements of ITO/SAM/SY/LiF/Al diodes. The LIXPS  $\Phi$ 's (eV) from Table 2-1 are shown.**

The diodes were then measured for their electroabsorption response. The electroabsorption spectra tend to be quite similar within this batch of devices, having all layers but the SAM being equal. Nominally, Equation 2-19 predicts that the red-shifted resonant peak in the electroabsorption response would scale linearly with  $V_{bi}$  due to the difference in  $\Phi$  of the ITO/SAM substrates. However, the actual intensity of the  $\Delta T/T$  spectrum is sensitive to the optical alignment of the experiment (described in the previous section), and so the relative proportionality of the spectral intensity for a series of devices such as these may be hard to fully characterize. However, this fluctuation in the actual  $\Delta T/T$  intensity between pixel alignments does not affect the  $V_{bi}$  that is measured; the intensity and slope for the bias-dependence can vary, but the intercept of the linear fit to the negative-bias regime will give the same  $V_{bi}$ , within standard deviation errors. The  $V_{bi}$ 's were measured for

two identically-prepared batches of these devices, one of which was from the same batch of substrates in which the  $\Phi$ 's were measured with LIXPS (Table 2-1). The  $V_{bi}$  was measured for three or more pixels per diode chip, one chip per SAM type per batch, for a total of six or more independent measurements of the  $V_{bi}$  per SAM type. The resulting mean is plotted in Figure 2-11 versus the LIXPS  $\Phi$ 's. The error bars for each axis indicate  $\pm$  one standard deviation.

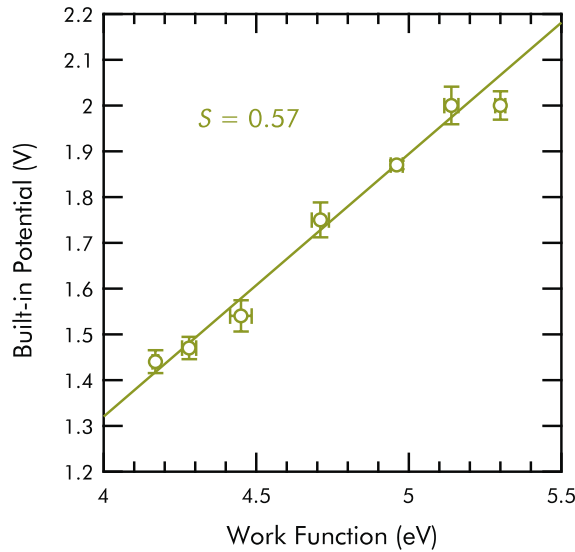


**Figure 2-11: Mean  $V_{bi}$  of ITO/SAM/Super Yellow/LiF/Al diodes versus the mean  $\Phi$  of ITO/SAM surfaces (prepared in the same batch as one of the batches of diodes used for electroabsorption) with vertical and horizontal error bars representing the standard deviation of the mean. Mean  $V_{bi}$  was taken from three or more pixels in each of two identically prepared batches of ITO/SAM/Super Yellow/LiF/Al diodes. The mean  $\Phi$  was taken from five spots on two or more samples of ITO/SAM surfaces (prepared in the same batch as one of the batches of diodes used for electroabsorption). A linear regression which omits the highest work function (due to presumed Fermi-level pinning) is shown with the magnitude of slope,  $S$ .**

The data in Figure 2-11 show a linear trend with an apparent saturation at high substrate work function: we observe a monotonic increase in  $V_{bi}$  as the work function of the substrate is increased over the range from 4.17 to 5.14 eV, but the  $V_{bi}$ 's for the substrates with the two highest work functions are the same ( $\sim 2.00$  V) within experimental error. We attribute this break in the linear trend at high  $\Phi$ 's to the Fermi-level pinning (also referred to as the

Bardeen limit, with slope  $S = 0$ )<sup>68</sup> that has been reported in many metal-semiconductor interface studies as the  $\Phi$  of the metal approaches the highest-occupied molecular orbital (HOMO) of the organic semiconductor.<sup>43,72</sup> UPS measurements of the ionization energy of SY on ITO put the SY HOMO edge at  $5.7 \pm 0.1$  eV (see Appendix A-5 for notes on the ionization energy and interfacial dipole formation). The data in Figure 2-11 are thus consistent with Fermi-level pinning occurring roughly half of an eV above the SY HOMO edge. Fermi-level pinning of the electrode several tenths of an eV above the HOMO edge (within the bulk gap) has been observed in many organic semiconductors, and is generally attributed to charge transfer to the tail of the density of states<sup>43,73</sup> within the gap. The absolute slope of proportionality between  $V_{bi}$  (or injection barrier, both illustrated in Figure 2-1) and  $\Phi$ , or “ $S$ ”, can be modeled with respect to the charge carrier concentration at the interface, described in great detail by Mönch<sup>74,75</sup>. Briefly, if states exist within the gap of the polymer that are equipotential with the vast density of Fermi states in the electrode, charge transfer can occur from the electrode to the density of interface states,  $D_{is}$ . The  $D_{is}$  can occur either from impurities or dopants, but have also been predicted to occur as an electrode-induced broadening of HOMO states<sup>74,76</sup>. When charge transfer to the  $D_{is}$  occurs, a space charge layer forms and results in a potential drop at the interface and the formation of an interfacial dipole. The magnitude of this interfacial dipole and the resulting  $S$  are therefore described as a parallel plate capacitor, in terms of the  $D_{is}$  (a function of the charge transfer density,  $Q_{is}$ ) and the separation between the metal states and the  $D_{is}$ ,  $\delta$ :

$$S = \frac{1}{1 + \frac{e}{\epsilon_i \epsilon_0} D_{is}(Q_{is}(\delta)) \delta} \quad 2-20$$

Equation 2-3 is a simple form of the derived interfacial slope parameter by Mönch<sup>74,75</sup>, with elementary charge  $e$ , the dielectric constant of the interface region  $\epsilon_i$ , and the

permittivity in vacuum  $\epsilon_i$ , and shows the inverse proportionality with  $D_{is}$ , which is also dependent on charge transfer density at  $\delta$ . The straight line in Figure 2-11 is a linear fit to the data with slope  $S = 0.57$ . In the ideal Schottky-Mott limit, when the dielectric layer is free of charge carriers,  $V_{bi}$  changes with the electrode  $\Phi$  with a unity slope, as there is not charge transfer states populated within the bandgap of the semiconductor. The sub-unity slope obtained here thus indicates a deviation from the Schottky-Mott limit for the interface between the SAM-modified ITO and the polymer. This deviation from the Schottky-Mott limit stands in contrast to both the general trend that “dirty” (e.g. non-UHV) solution-processed metal/organic interfaces tend to exhibit Schottky-Mott behavior,<sup>43</sup> and specifically to the previous reports of  $V_{bi}$  made using electroabsorption on a series of SAM-modified coinage metal electrodes that found Schottky-Mott behavior.<sup>44,51</sup>

To our knowledge, these are the first systematic measurements of  $V_{bi}$  as a function of  $\Phi$  made for a SAM-modified TCO contacts. The observed sub-unity slope could be explained by a number of possible physical models. For instance, the induced density of interface states (IDIS) model<sup>74,76</sup> indicates that a density of states within the semiconductor gap equal to  $\sim 5 \times 10^{13} \text{ cm}^{-2}$  is sufficient to bring the slope/proportionality between  $V_{bi}$  and  $\Phi$  below unity, as the slope is given to be inversely proportional to the density of interface states.<sup>43</sup> In this case, one would like to explain the origin of these interfacial states. We note that while this is an open question in the field, the states do not appear to be intrinsic to the SY polymer (we also observed deviation from the Schottky-Mott limit for a polyfluorene, Appendix A-4). We note that the density of states required to observe a sub-unity slope is on the order of SAM coverage density on ITO for the  $\Phi$  we measure here (previously estimated to be  $2 \times 10^{13}$  to  $1 \times 10^{14} \text{ cm}^{-2}$ )<sup>48,77</sup> perhaps indicating a role of the SAM molecules in the interfacial state formation. The observation of a Schottky-Mott behavior in previous work,

using different SAMs, also points to a potential role for the SAM. We speculate that the fluorinated SAM may serve to reduce atmospheric/process contamination prior to the polymer being spincoated, and that the relatively-thin SAM layer does not inhibit electronic overlap between electronic states in the ITO and a density of interface states in the organic. Alternatively, we speculate that the PA's used here may have  $\pi$ - $\pi$  interaction with the conjugated polymers. Finally, we note that the strong dipole interactions of the SAM layer could influence the solid-state order of the first monolayer of solution-processed polymers during spincoating, leading to an oriented interface layer with a partially counteracting dipole. Further detailed experiments will be required to distinguish between these hypotheses.



## **CHAPTER 3:**

### **Charge modulation spectroscopy plasmonic nanoparticles**

#### **3-1. Introduction**

Plasmonic metal nanoparticle enhanced optoelectronic applications such as LEDs<sup>78</sup>, lasers<sup>79</sup>, photodiodes<sup>80</sup>, and biosensing devices<sup>81</sup> are based on the unique properties of localized surface plasmon resonances, i.e., light driven collective oscillations of conductive electrons at a metal/dielectric interface, giving rise to light concentration and scattering effects at the nanoscale<sup>82</sup>. Enhanced light harvesting using plasmon resonant metal nanostructures is, therefore, one promising route to improve light absorption in optically thin OPV films.<sup>83</sup>

The inclusion of metal nanoparticles into organic BHJs was proved to lead to plasmon-enhanced absorption and charge generation, an increase in photocurrent and charge-carrier mobility and even an increase of the overall power conversion efficiency.<sup>84-92</sup> However, negative results, i.e., reduced power conversion efficiency and minor, often not understood effects, have also been reported.<sup>91,93</sup> The exact mechanism of enhanced performance in OPV devices remains in part unclear. It could arise from enhanced near-field absorption, light scattering leading to increased path lengths, or in some cases it could simply be enhanced electrode roughness leading to larger internal surface areas. In some cases, the metal nanoparticles may simply form an additional transportation network, thereby, improving the electrical conductivity of the OPV layer.<sup>21,91</sup> A recent study suggests that photoinduced oxidation of PEDT:PSS due to the presence of silver nanoparticles may also contribute to the enhancement of organic solar cell performance.<sup>94</sup> Hence, a fundamental understanding of the

mechanisms of efficiency enhancement or what might prevent it is an important prerequisite for effectively employing metal nanostructures for light trapping in thin-film solar cells.

Recently, our group found significant enhancement of charge carrier yields in poly(3-hexylthiophene):[60]PCBM BHJ blends when deposited onto films of plasmon-resonant silver nanoprisms (AgNPs), with photoinduced absorption (PIA) detecting polaron yield enhancements up to  $\times 3$ .<sup>95</sup> Such an enhancement is described as the increase in the absorption of long-lived positively-charged polarons within P3HT domains, identified as a negative resonance of the  $\Delta T/T$  PIA spectrum at  $\sim 1.25$  eV (shown as increasing with optical density of the AgNP layer in Figure 3-1). On the other hand, it was observed that in the presence of AgNPs, the PIA spectrum of the BHJ blend changed dramatically after photoexcitation in the region around the AgNP's localized surface plasmon resonance (LSPR). Figure 3-1 shows that as the OD of the AgNP layer is increased, an inversion happens in the PIA spectrum, resulting in an absorption enhancement (bleach) at higher (lower) energies than the AgNP's LSPR (1.95 eV for that particular batch). It was hypothesized that the changes in the PIA spectrum were due to electron accumulation on (photoreduction of) the AgNPs. In a plasmonic OPV device this could represent a path for charge recombination. This would then affect  $V_{oc}$ , charge carrier extraction, and therefore lowering the overall power conversion efficiency. We use CMS on capacitive (non-OPV) devices to positively identify this previously-observed spectral fingerprint; upon photoexcitation, AgNPs are loaded with negative charge carriers (electrons), leading to a blue-shift of the AgNP plasmon resonance. Two different approaches to prevent electron charging of the AgNPs are then proposed.

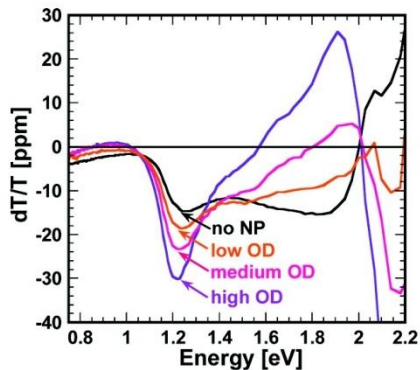


Figure 3-1: Adapted with permission from Kulkarni, A. P.; Noone, K. M.; Munchika, K.; Guyer, S. R.; Ginger, D. S. Plasmon-Enhanced Charge Carrier Generation in Organic Photovoltaic Films Using Silver Nanoprisms. *Nano Letters* 2010, 10, pp. 1501–1505. Copyright 2010 American Chemical Society. The PIA spectra are shown for P3HT:PCBM films of the same thickness, deposited onto AgNPs of varied optical density (OD). The plasmon resonance for these AgNPs occurs at  $\sim 2$  eV.

### 3-2. Sample preparation

To specify the carrier type that charges the AgNPs in the previous work, we need to incorporate the AgNPs into a structure between two electrodes, but which only can inject/extract carriers from one electrode. The methods for preparation of the AgNPs and their attachment to substrates are described in the previous work: Kulkarni et al.<sup>95</sup> ITO slides (being previously described in Section 2-2) that were treated with 3-aminopropyltrimethoxysilane (APTMS) were submersed in the colloidal AgNP solution for 24-48 hours. AgNPs lay flat on the ITO, are on the order of 100 nm in edge length (depending on the synthesis), standing  $\sim 5$  nm tall. After assembly on the ITO, the AgNPs were overcoated with a 200 nm thick layer of SiO, on top of which a 100 nm thick Al metal electrode was deposited (100 nm). The dielectric SiO layer prevents charge transfer between AgNPs and Al when applying a bias; charge injection can only occur through the ITO electrode. Other control devices were similarly prepared and with differences described in the following section.

### 3-3. Results and discussion

The experimental apparatus for CMS is identical to that of the EAS experiments. The primary difference in performing CMS is the device structures and operating conditions that are implemented. We therefore forego an entire section dedicated to the practical application of the technique, and instead list practical notes that are particular to this implementation when applicable. In order to specify the carrier type that charges the AgNPs, we need to incorporate the AgNPs into a structure which only can inject/extract carriers from one electrode. The CMS sample structure (not to scale) is illustrated in an experimental schematic in Figure 3-2. To test the hypothesis posed by Kulkarni et al.,<sup>95</sup> we probed the AgNP samples near their LSPR, with  $\Delta T/T$  spectra indicated changes in the LSPR due to charging.

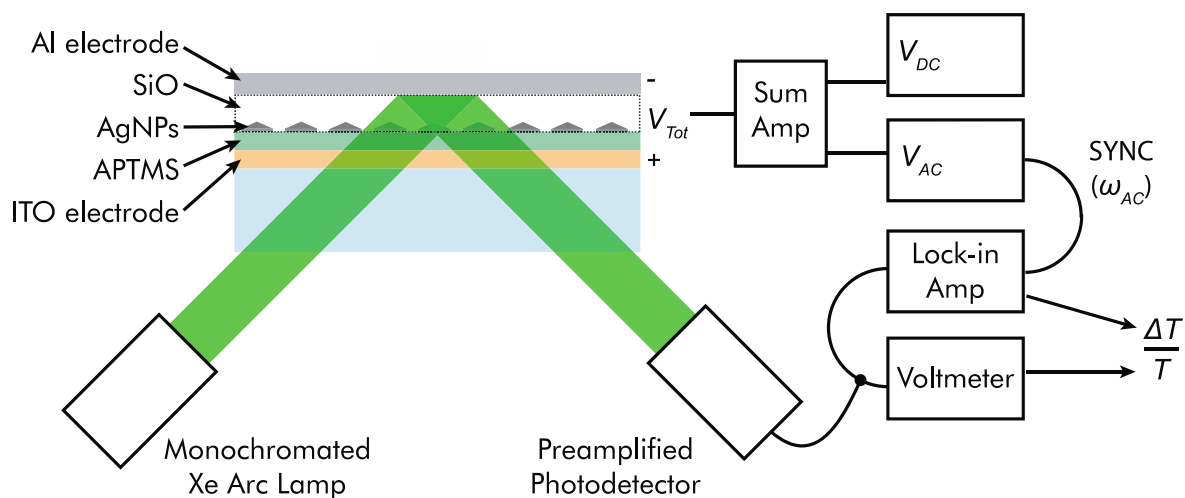
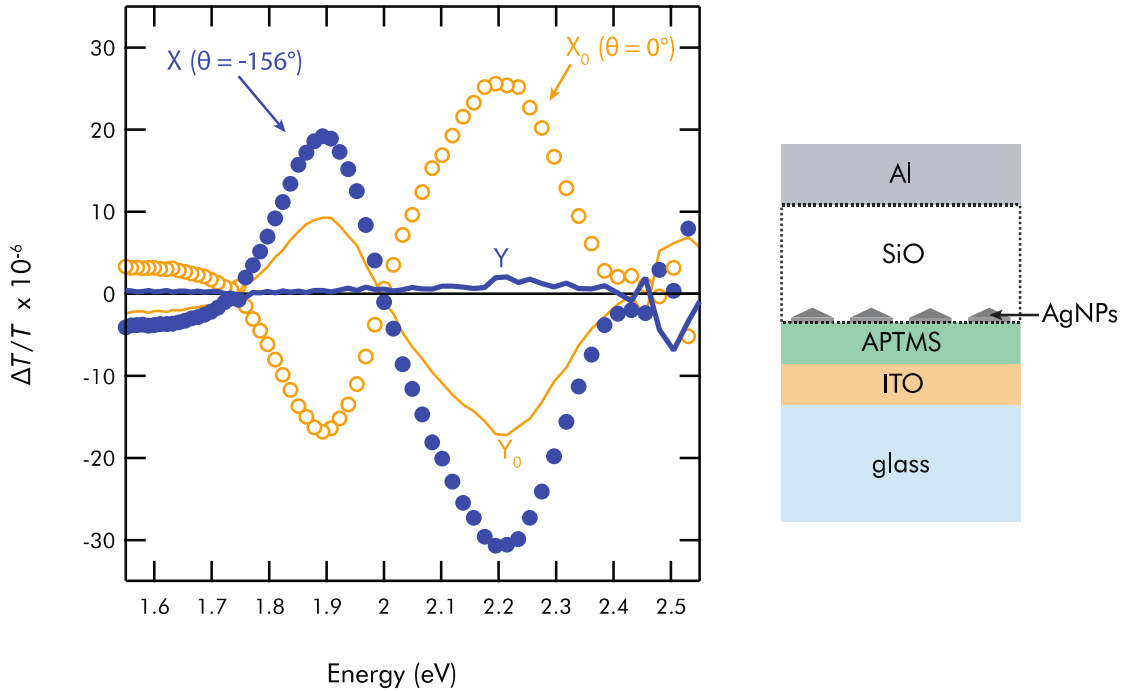


Figure 3-2: Schematic of the CMS experiment showing a device under test. The SiO layer prevents charge injection/extraction to the AgNPs from the Al electrode. The AgNPs lay flat on the APTMS binder layer.

With the biasing convention shown in Figure 3-2, the bias is applied to the ITO electrode with respect to the reference potential being applied to the Al electrode. For all CMS data

represented in this dissertation the probe bias was at 4 V AC (peak-to-peak) and -10 V DC, near the maximum unsaturated output of the custom-built summing amplifier. However, the sign and magnitude of the DC bias seemed to have little, if any, influence on the spectral intensity or shape, and so future experiments may benefit from increased signal by using larger AC voltages and smaller DC voltages. When the lock-in amplifier is phase-locked to the function generator and at  $\omega_{AC}t = (2n\pi + \pi/2)$ , the AC sine wave being applied to the device structure causes the ITO to be at a more positive potential with respect to the Al electrode than at  $\omega_{AC}t = (2n\pi)$ , when the sine wave is at zero amplitude. In this case, a completely positive (negative) in-phase component of the lock-in amplifier output,  $\Delta T$ , would be a bleach that is due to positive (negative) charging from the ITO electrode. Figure 3-3 shows the fractional change in transmittance that was measured for the ITO/APTMS/AgNP/SiO/Al structure. With the lock-in amplifier set to have no offset in phase ( $\theta = 0^\circ$ ), the fractional change in transmittance at 2.2 eV is mostly positive and in-phase ( $X_0$ ), but with some negative quadrature intensity ( $Y_0$ ). This corresponds to charge-modulated bleaching at 2.2 eV when the AgNPs are more positively charged. The nonzero quadrature component is attributed to the phase-lag response of the electronic circuitry of the experimental apparatus. In order to account for this lag, we then set a phase offset to make a mostly in-phase response completely in-phase and positive. For this particular sample,  $\theta = +24^\circ$  will eliminate the quadrature response. However, in the interest of describing the change in transmittance due to putting the ITO at more negative potential, we can add an additional phase offset of  $\theta = -180^\circ$  (following from the logic above). For the data presented in this dissertation, such phase rotations were performed by manually “rotating” the in-phase/quadrature data after the measurements were performed, because the optimal phase assignment was not known at the time of the experiment. In practice, this phase offset can be set at the time of the experiment, with prior knowledge of the sample response.

Applying this phase rotation, the resulting in-phase response ( $X$ , blue filled circles) with negligible quadrature response ( $Y$ , bold blue line) is shown in Figure 3-3 with the zero-phase data. The CMS spectra are reported in eV, following the convention of the previous PIA studies.



**Figure 3-3: The charge-modulated change in transmittance for the structure at right. The open orange circles are the in-phase response ( $X_0$ ) and the fine orange line is the quadrature response ( $Y_0$ ) when probed with zero phase offset. The filled blue circles are the in-phase response ( $X$ ) and the bold blue line is the quadrature response ( $Y$ ) upon rotating the lock-in phase by  $\theta = -156^\circ$ .**

In Figure 3-4 the phase-rotated in-phase response of the charge-modulated AgNP structure is re-plotted with the absorbance spectrum for the AgNPs in an glass/ITO/APTMS/AgNP/SiO structure. The SiO layer is necessary to accurately represent the plasmon resonance due to its dependence on the surrounding dielectric environment. After assigning the phase response of the CMS experiment, we see that indeed, the AgNPs exhibit an increase in absorbance ( $-\Delta T/T$ ) at probe energies above the AgNP plasmon

resonance when the ITO electrode is made more negative, suggesting that the previously observed photo-induced reduced absorption was due to electron-charging of the AgNPs. The corresponding bleach ( $+\Delta T/T$ ) at probe energies below AgNP plasmon resonance follows with the expected derivative line shape from the difference of extinction spectra between “neutral” (shown as red dots in Figure 3-4) and “charged” AgNP plasmons. While we expected that the intensity of applied fields were not high enough to cause electroabsorption of the AgNPs, we devised several control structures to confirm the nature of the modulated response; the structures are shown in the legend/top of Figure 3-4. The first structure is identical to that described in the previous section (and depicted in Figure 3-3), but that it was not soaked in the AgNPs solution (w/o AgNPs). When probed under the same test conditions, the modulated response of this control was rather small, barely above the detectable limit of the apparatus, but shared a low-energy feature (from  $\sim 1.55$ - $1.7$  eV). This result suggests that the large modulated response observed was due to the AgNPs bound to the surface. However, it wasn't certain what the low-energy feature was due to. The second control (supernatant) was also identical to the structure with AgNPs, but it was soaked in the supernatant of the AgNP synthesis, rather than the AgNP solution. The inclusion of this sample was to check that the charge-modulated response (or possibly an electroabsorption response) was not due to any possible residuals from the synthesis. The response from the supernatant control was also barely above the noise floor – both the supernatant control and the control w/o AgNPs sample responses were smoothed in post-processing to aid in the visual comparison. The supernatant control also shared the low-energy feature with the Ag-NPs sample. The third control, the SiO-sandwich structure, was also prepared identically to the AgNPs structure, but a second SiO layer was added to the vertical assembly, before adding the APTMS binder layer. This SiO-sandwich behaved quite similarly to the first two controls, lacking the large modulated double-feature from  $\sim 1.75$ - $2.45$  eV seen in the original AgNP structure. Because

this sample also contained the AgNPs, but electrically insulated them from both contacts, it seems that neither the AgNPs nor the APTMS contribute a significant electroabsorption response. However, the low energy feature was still present and unidentified.

As further proof of our charge-modulated assignment, we performed measurements on structures similar to the standard AgNPs structure (Figure 3-3), but with batches of AgNPs from different syntheses, with different plasmon resonances. The measurements were performed under the same biasing conditions. The modulated transmittance response shifts with the extinction peak of the AgNP films, corroborating with assignment of the electromodulated response as being to electrically-driven reduction of the AgNPs, resulting in a small blue-shift in the plasmon resonance of the AgNPs. The verification of the hypothesis put forth by Kulkarni et al. suggests that if plasmonic AgNPs are to be incorporated in BHJ OPVs for their absorption enhancement affects, they should be electrically insulated to prevent charging from photogenerated electrons, which would pose a loss mechanism to rapid collection of photogenerated free carriers.

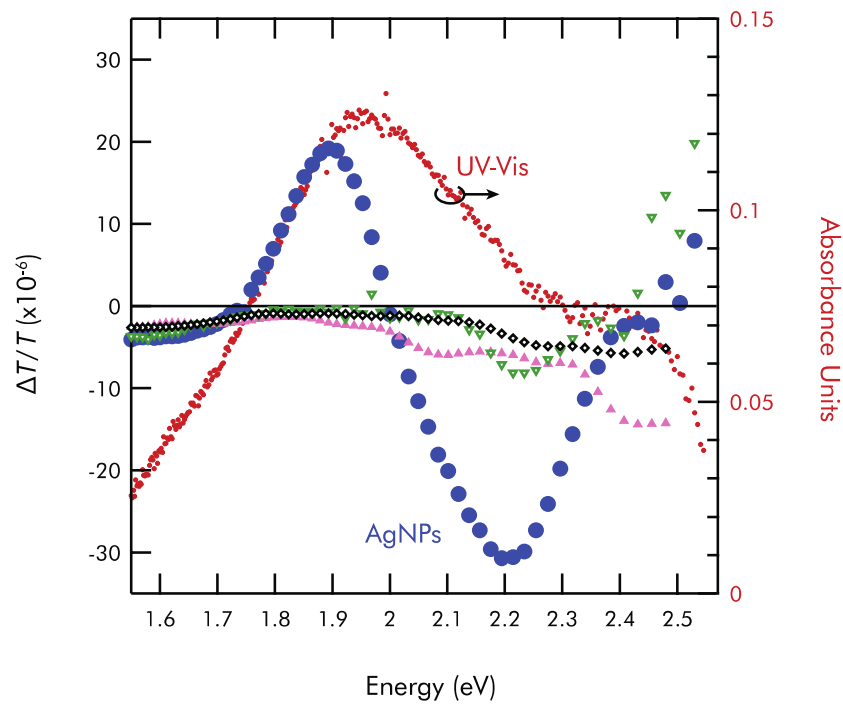
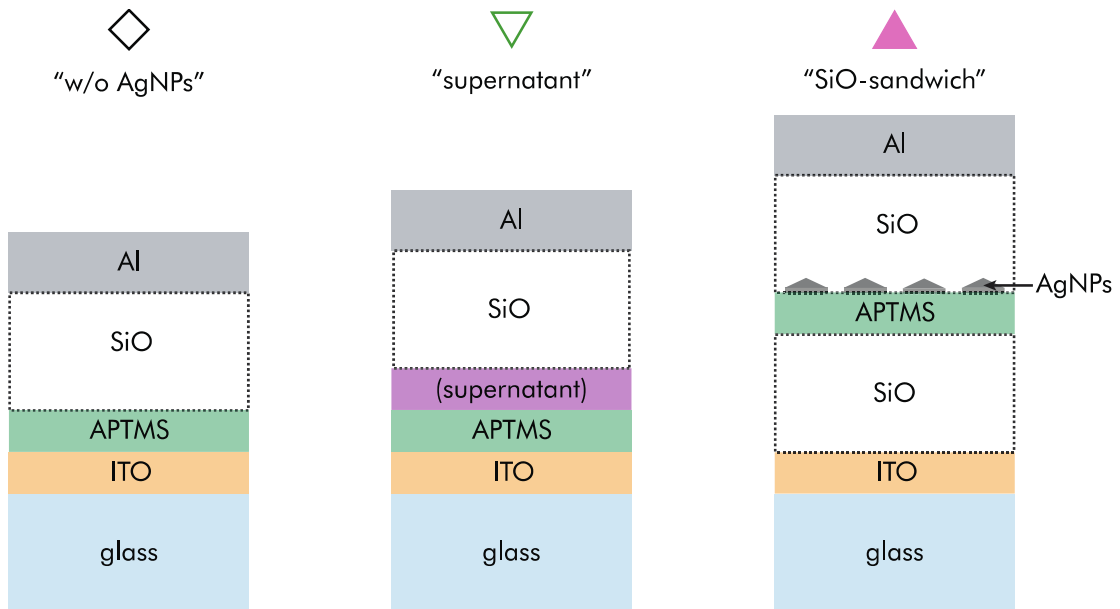


**Figure 3-4:** Legend for the three control structures: (Top Left) no AgNPs, (Top Middle) supernatant soak, (Top Right) SiO-sandwich. (Bottom) The in-phase response for the control structures are shown on the left axis with the AgNP in-phase response, already displayed in Figure 3-3. For spectral reference, the right axis shows the absorbance measured an ITO/APTMS/AgNP/SiO structure for this batch of AgNPs. All modulated spectra were recorded at 4 V AC (peak-to-peak), -10 V DC and are displayed with a post-processed phase offset of  $\theta = -156^\circ$ .

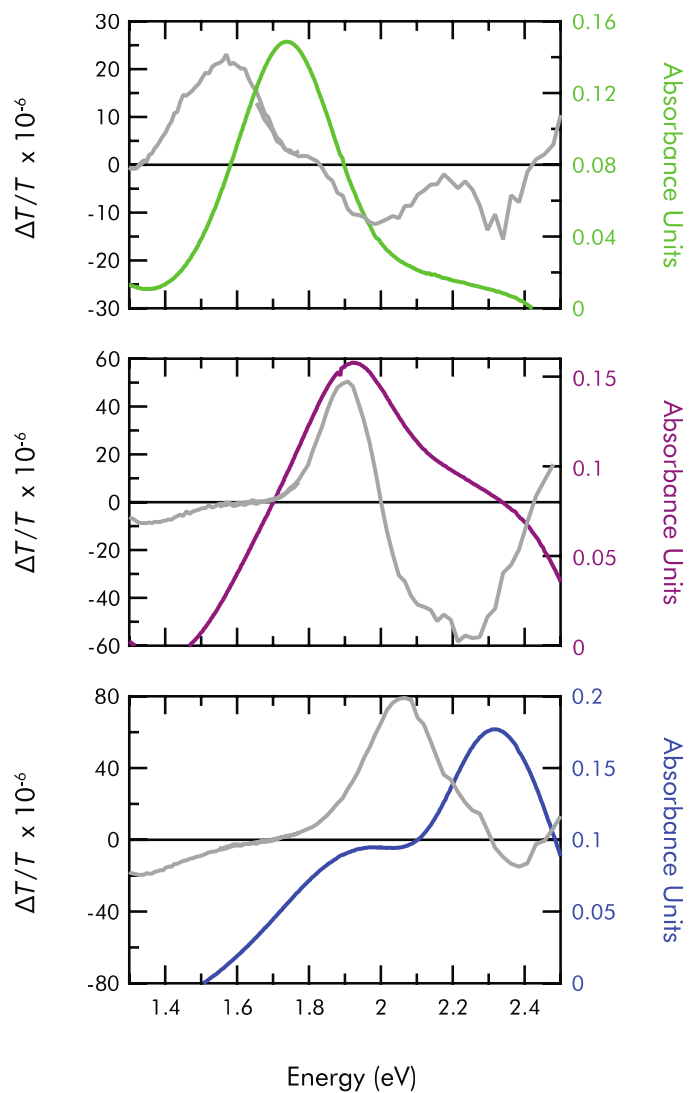


**Figure 3-5: Charge-modulated transmitted spectra (grey lines) and corresponding extinction spectra (colored lines) for AgNP samples with resonances throughout the visible spectral region in the structure glass/ITO/AgNPs/SiO/Al. The CMS signal shifts in the same direction as the plasmon resonance of the AgNPs.**

## CHAPTER 4: Conclusions and future directions

### 4-1. Achievements

An apparatus was constructed to perform electrically-modulated transmittance spectroscopy on organic semiconductor diodes and OPV-relevant device structures. The goal was to investigate interfaces within these devices and to do so non-invasively in electronically similar modes of operation to those which exist in function devices – which is not possible in many surface science techniques which attempt to probe similar device physics. We first performed a systematic study on organic polymer-based diodes in which we tuned the transparent conducting oxide using dipolar PA SAMs. Previous work had shown that electronic properties (such as  $\Phi$ ) could be tuned with these PAs and that devices fabricated with the functionalized ITO could also be improved. We functionalized ITO surfaces with the PA SAMs and characterized the trend in  $\Phi$  using LIXPS, seeing excellent qualitative agreement with previous trends. When we fabricated organic diodes from the functionalized ITO, we observed that the larger- $\Phi$  modified-ITO produced larger injection currents in polymer diodes, commensurate with the expected reduction in hole-injection barrier from ITO to the polymer hole-transport energy levels. Further, the EAS-measured  $V_{bi}$ 's trended linearly with our LIXPS-measured  $\Phi$ 's. The slope of the proportionality between these two values was sub-unity, indicating deviation from the Schottky-Mott limit, or the formation of an interfacial dipole due to an interfacial charge transfer. Such a systematic study using EAS to measure  $V_{bi}$  when the TCO electrode was modified with a dipolar SAM has not previously been reported. To our knowledge, the observed behavior had

also not previously been reported for organic semiconductors being solution coated onto electrodes in ambient conditions, regardless of the experimental technique used (EAS or UPS). This is interesting because it indicates a cleaner interface is formed, one which allows for a greater degree of electronic overlap between states in the TCO electrode and the polymer layer, that has been seen for solution-coated systems in the past. Previous reports of this behavior were attributed to electrode/organic systems processed in UHV systems, which are not as favorable of conditions for fabrication of low-cost organic electronics such as OLEDs and OPVs. This suggests that the PA SAM modification of TCOs may produce a more robust electrical contact for future solution-coated OPVs.

The second line of investigation used CMS to identify the charging behavior of plasmon resonant AgNPs. Prior to this study, it was observed that these AgNPs could improve carrier generation in BHJ blends, but PIA spectroscopy showed a fingerprint which would likely lead to carrier recombination for BHJ devices. We verified that when the AgNPs were reduced with electromodulation, our spectroscopic technique, CMS, gave the same fingerprint. Therefore it will be necessary to insulate these nanoprisms from the donor-acceptor materials in the BHJ if they are to be incorporated for their absorption enhancement properties. We are preparing to report on the CMS measurements in conjunction with PIA measurements performed on BHJ films. In one instance the thickness of an insulating overlayer (much like the SiO used in CHAPTER 3) will be varied, and in a second, the AgNPs will be directly coated with an insulating shell. Due to the prolific nature of plasmonic nanoparticles in OPV research, this will undoubtedly be the focus of future work.

## 4-2. Suggested directions for EAS and PA SAMs

Many of the early efforts in this investigation seemed to be plagued with inconsistency. It seems that the short timescale dynamics and surface chemistry that occur on oxides between oxygen plasma cleaning and exposure to ambient conditions may impede the successful assembly of PA monolayers. Further, of the several research groups working with these PA SAMs on oxide surfaces, none seem to have agreed upon the ideal depositions technique: T-BAG<sup>48,96</sup>, soaking<sup>49,97-99</sup> and microcontact printing<sup>50</sup> have all been used and with various ITO cleaning/prepping, PA material concentrations, process solvents, incubation periods, incubation temperatures, and with(out) post-treatment steps such as heating and drying. Is there a more reproducible method for the self-assembly of PAs that has not yet been reported, or is one truly superior? Characterizing the structures formed is not trivial within the constraints of time and cost. Inexpensive and rapid methods such as contact angle measurement (via sessile drop method) can give quick qualitative information but are not robust enough to characterize the coverage density of the SAM. Ambient Kelvin probe potentiometry can be performed rapidly, but the absolute values of  $\Phi$  tend to vary significantly from those measured with photoelectron techniques, and may not be as relevant to the potentials that charges take-on in an operational device. Any technique which requires a UHV conditions will not result in a rapid/inexpensive characterization of the SAM. While many of the current studies using the Marder group materials are novel and attempt to understand the formation of the SAM itself, perhaps future efforts in the systematic study of dipolar PA SAMs on oxides should be spear-headed with an effort to normalize the deposition and yield-verification, focusing on the methods of fabrication, rather than the methods of characterization.

This deviation from the Schottky-Mott limit was observed for two different polymer systems (SY and PFO) on similar systematic studies where the PA SAMs were used to the effective ITO work function over a range in excess of 1 eV, while the third polymer, P3HT, appeared to be always pinned to the P3HT HOMO, regardless of the modified-ITO  $\Phi$ . The slope parameters measured for these two polymers were both less than the Schottky-Mott limit, but were statistically different. That the effect could not be tied directly to only one of the polymers and that similarly processed polymer-on-electrode systems typically display Schottky-Mott behavior suggests that this deviation may be unique to this particular interface of study: oxide/dipolar SAM/polymer. Due to the complexity of performing such extensive studies, we were not able to answer all of the questions that tend to arise during experimentation, such as: was the difference in  $S$  (slope) for these two polymers due to properties of the polymer, the SAM quality (coverage density achieved in each experiment), or some complex interfacial species? Perhaps similar studies with additional organic semiconductors, even thermally evaporated small molecules, may elucidate this matter.

## APPENDIX A: Appendix to CHAPTER 2

### A-1. Equipment photos

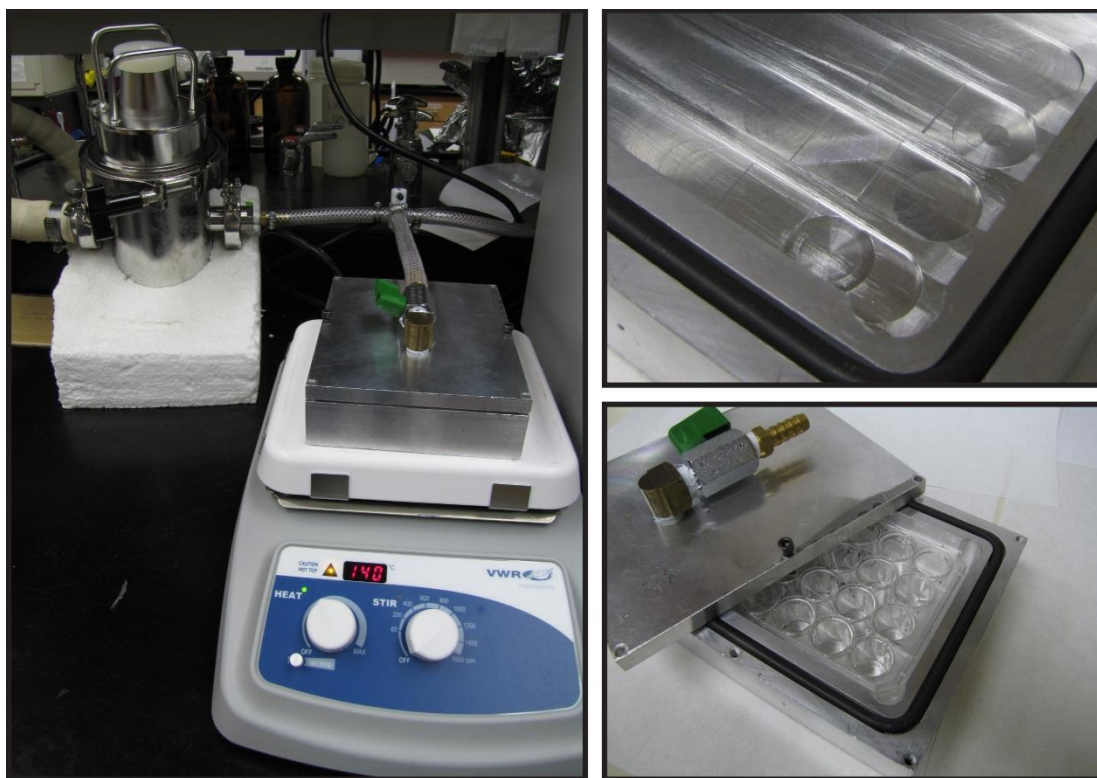


Figure A-1: (Left) Custom-built vacuum annealing box with liquid nitrogen vacuum trap. (Top right) Grooves for positioning ITO substrates. (Bottom right) Vacuum box being used to store samples under static vacuum in a Multiwell container.

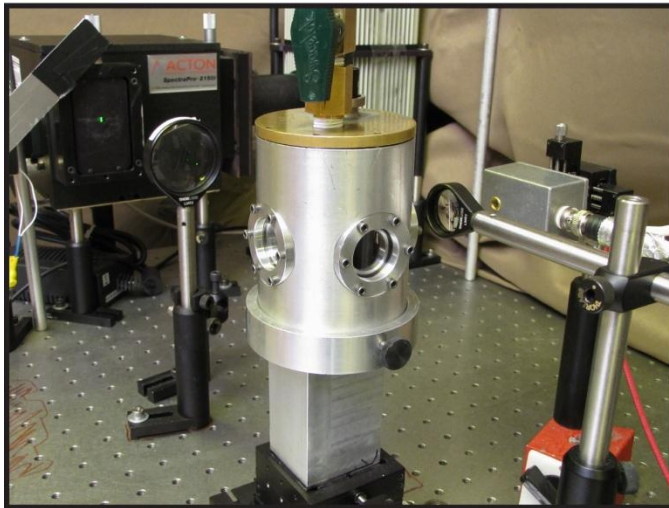


Figure A-2: (Top) The custom-built electroabsorption apparatus. (Bottom left) Close-up of the vacuum test chamber, showing the geometry of the optical probe and detection. (Bottom right) Device holder with 8-pixel Super Yellow diode chip.

## A-2. Diode conditioning

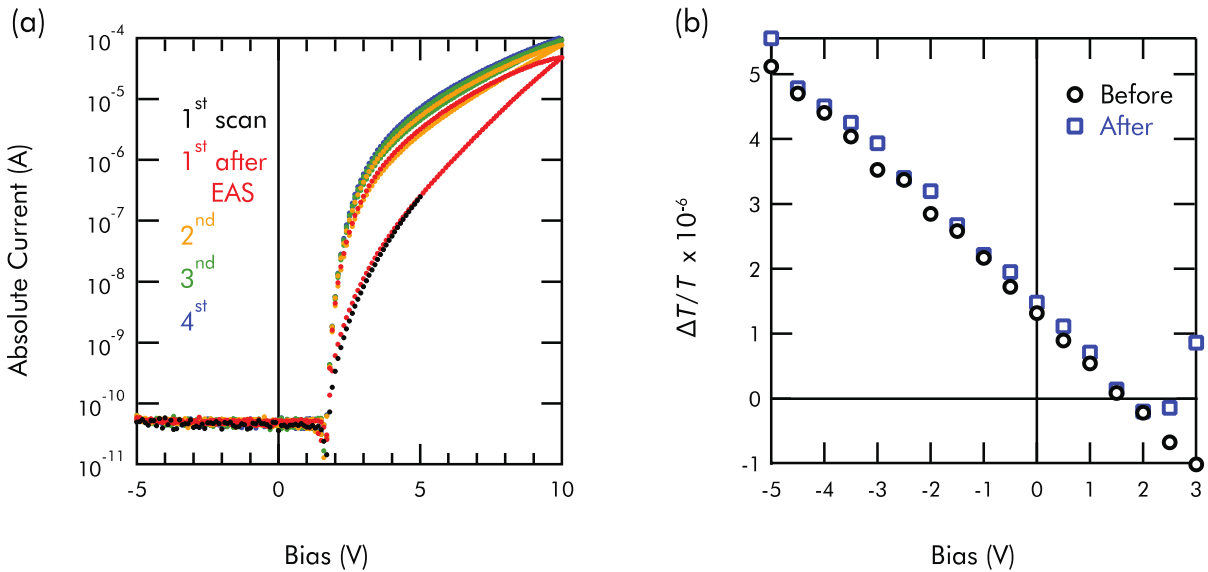


Figure A-3: Measurements on a typical ITO/pCF<sub>3</sub>/SY/LiF/Al diode: (a) Dark current-voltage measurements where the first scan was made from -5 to +5 V (black) before electroabsorption measurement and then rescanned from -5 to +10 to -5 V after the electroabsorption measurement (red). Subsequent scans from -5 to +10 to -5 V show slightly increasing injection currents under forward bias, with slightly higher current magnitude when sweeping from more positive to more negative bias. (b) Electroabsorption measurement on the same diode showing the voltage dependence before and after the diode had been biased to +10 V.

We observed that biasing diodes of the structure shown in Figure 2-4 could result in an irreversible change to the current-voltage response, when the forward bias was significantly large, and consequently, when the device passed significant currents. If the device was not biased at a high enough forward voltage the change was not observed and the same current-voltage response would be measured, repeatedly and with negligible hysteresis (represented as the black dots and red dots, up to +5 V in Figure A-3a). Figure A-3a shows a changing behavior for a SY diode that was fabricated similarly to those described in the main text of this dissertation, but that the actual thickness of the SY layer was measured at 128 nm by profilometry; we note that the observations for this slightly thicker polymer layer are qualitatively similar to devices reported in the main text. This current conditioning effect was always irreversible and resulted in more of a space-charge-limited current response. The

current conditioning of SY diodes also resulted in a change to the bias-dependent electroabsorption measurements. Figure A-3b shows the difference; prior to conditioning, the response is fairly linear over the typical range of biasing used to determine the built-in potential ( $V_{bi}$ ). However, after the device is current conditioned, a charge modulation feature is observed at forward bias; the bias-dependence of  $\Delta T/T$  is linearly decreasing with increasingly positive bias but increases exponentially at and above near- $V_{bi}$  conditions, as described in the manuscript. Prior to implementing this current-conditioning procedure, the electroabsorption voltage response for SY diodes with large work  $\Phi$  PA SAM-modified ITO electrodes would display response similar to both traces shown in Figure A-3b, seeming to vary with the batch of samples being prepared. It was always observed in batches of diodes where large  $\Phi$  substrates showed a charge modulation feature under positive DC biasing that sufficiently-low  $\Phi$  substrates would not show the same charge-modulated response. However, some batches of diodes did not show a charge-modulated response for any of the devices, regardless of the size of substrate  $\Phi$ . This current-conditioning is not fully understood, but does lead to a more-reproducible device characterization response. There are many hypotheses that could be proposed for the observed responses. Filling of deep charge traps from defects or interface states with the substrate, or potential-activated electrochemical reactions of the polymer are possible explanations for this observed increase in injected current levels and charge-modulated changes in transmittance, but further experimentation would be required to isolate the cause of the observed responses. Perhaps a systematic study of the temperature-dependent current-voltage and electromodulated responses for diodes being conditioned in a similar manner would fully resolve the chemistry that occurs in devices under operation.

### A-3. Phosphonic acids from the Marder group

The PAs used in these experiments were synthesized by Anthony J. Giordano and Peter J. Hotchkiss and come from the following batches:

oF<sub>2</sub>: AJG-II-295A or PJH-III-132a

BnPA: AJG-II-159

mpF<sub>3</sub>: PJH-III-043B

pF: PJH-III-072A

F<sub>5</sub>: PJH-III-165 or PJH-II-65A

pCF<sub>3</sub>: AJG-II-298A or PJH-III-73d

### A-4. $V_{bi}$ in other polymer systems

Similar to studies described in CHAPTER 2 with SY polymer, electroabsorption was performed on diodes made with the polymers poly(3-hexylthiophene) (P3HT, Rieke Metals, Inc. Sepiolid P100) and polyfluorene (PFO, American Dye Source, Inc. 129BE), with structures shown in Figure A-4. These measurements predate the diode conditioning discoveries (Appendix A-2) and the independent measurement of  $\Phi$ 's using LIXPS (Section 2-3), and therefore are placed in the Appendix to support the more well-controlled measurements using the SY polymer. We show the data here to support the observations of a sub-unity slope observed for the SY diodes described in CHAPTER 2; PA SAM diodes with PFO also show a sub-unity slope and PA SAM diodes with P3HT appear to exhibit Fermi-level pinning for the entire range of  $\Phi$  modification. The deposition for the PA SAMs on ITO done in these earlier studies were slightly varied in methods and they were fabricated before

some sources of surface contamination (lower SAM coverage densities) were identified, mainly the O-ring contamination characterized in Section A-9. Further, the measurement of  $\Phi$  for the SAMs used in the earlier studies was not performed at the time of those studies and therefore, we use the values of  $\Phi$  which were measured in accordance with the SY polymer diode studies of CHAPTER 2, and admit that errors are unknown but that these values represent the best guesses. We describe in this section how the methods for preparing these samples varied from the description given in Section 2-2.

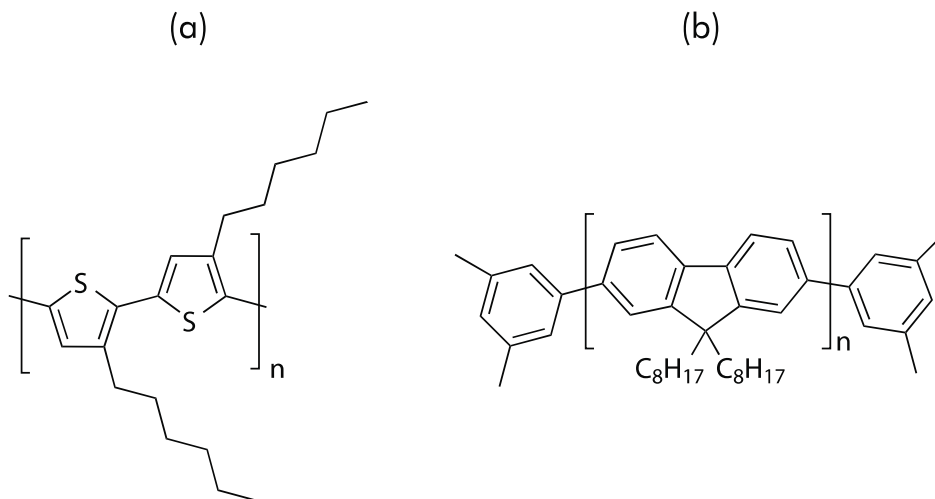


**Figure A-4: (a) poly(3-hexylthiophene) (P3HT) and (b) polyfluorene (PFO)**

Notes for P3HT diodes appear in Noah Horwitz lab book #2, starting on p. 200. For P3HT diodes, ITO was prepared similar to what was described in Section 2-2, but the plasma cleaning was done with air plasma and the Harrick set to 18 W power (predating the metered oxygen process gas capabilities), for a 15 minute duration. The SAMs were deposited similar to “tethering by growth and aggregation” (TBAG) method<sup>96</sup> using a 1 mM ethanolic solution. Briefly, the samples were submersed in a reaction vial with the 1 mM PA solutions, but left unsealed and in a fume hood, where the full evaporation of the ethanol would occur in

approximately 4 hours. This method required more rigorous cleaning to remove multilayer PA residuals (PAs that were physisorbed on top of the first chemisorbed monolayer); this was done with 30 minutes of ultrasonication in ethanol, 30 minutes ultrasonication in 5 vol % triethylamine in ethanol (described in Section 0), and drying with nitrogen gas. The samples were then annealed for 24 hours at 140 °C, covered at laboratory atmosphere (predating the custom vacuum annealing & drying chamber depicted in Section A-1 and described in the process of Section 2-2). After cooling, samples were transferred to the nitrogen glovebox environment, and P3HT films were spincoated from 25 mg/mL solutions with chlorobenzene, being kept at 60 °C. After solids were completely dissolved, the solution was filtered with 0.2 µm PTFE filter, and returned to heated stirring. 70 µL of the solution was spread onto the substrate and the spincoater process was immediately started: 1750 RPM for 2 minutes with acceleration setting at 424 RPM/sec. Spincoating with similar settings yielded nominal thicknesses of ~100 nm. P3HT diodes were finished by thermally depositing 90 nm of Ca, venting to swap evaporation sources, and thermally depositing 50 nm of Au. Voltage-dependent EAS was performed at 640 nm wavelength.

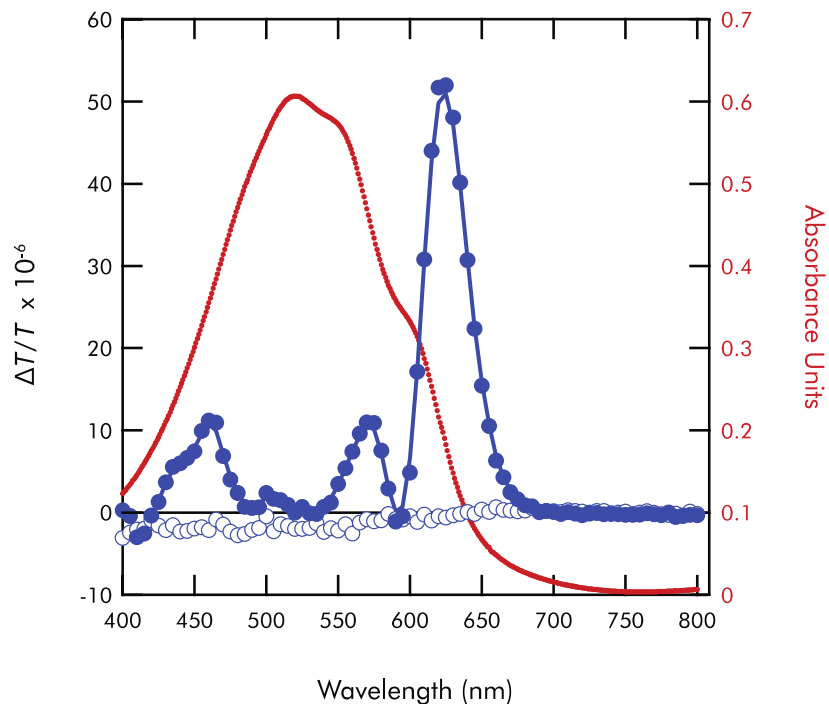


**Figure A-5:** The absorbance of a P3HT film is shown in the red dots on the scale of the right axis. The electroabsorption spectrum of a diode made from the same film and of structure ITO/P3HT/Al, is shown on the scale of the left axis. The blue-filled circles are the in-phase response, with line as a guide to the eye, and the blue unfilled circles are the negligible quadrature response. These electroabsorption spectra were recorded at -2 V DC, 0.2 V AC (peak-to-peak). Data located in group data storage at \\Bradley MacLeod\Data\BM6\BM6\_111\_x121 - EA P3HT PA SAMs\Batch #1\.

Notes for PFO diodes appear in Noah Horwitz lab book #3, starting on p. 31. The SAM deposition for PFO diodes more closely followed that reported in CHAPTER 2, utilizing a soak at elevated temperature, rather than the TBAG method. ITO was detergent and solvent cleaned and air plasma cleaned for 5 minutes on the 18 W power setting (also predating the metered oxygen process capabilities). The ITO substrates were immediately submersed in 10 mM ethanolic solutions of PAs at 75 °C, and incubated for 2 hours. These PA SAMs were also ultrasonicated with 5 vol % triethylamine in ethanol for 30 minutes, rinsed with ethanol, nitrogen-dried, and annealed for 2 hours at 140 °C, covered at laboratory atmosphere. After cooling, samples were transferred to the nitrogen glovebox, and PFO films were spincoated from 25 mg/mL solutions with chlorobenzene, being stirred and kept at 60 °C. After solids were completely dissolved, the solution was filtered with cascaded 0.45 μm and 0.2 μm

PTFE filters, and returned to heated stirring. 80  $\mu\text{L}$  of the solution was spread onto the substrate and the spincoater process was immediately started: 2500 RPM for 2 minutes with acceleration setting at 13,568 RPM/sec (the maximum setting). Spincoating yielded nominal thicknesses of  $\sim 100$  nm. Films were annealed under vacuum (using the custom chamber) for 30 minutes at 125  $^{\circ}\text{C}$ ; this step was performed in analog with the annealing of active layer materials used in organic photovoltaics, but was not verified to result in any superior qualities for these single layer devices. Films were cooled under static vacuum overnight. PFO diodes were finished by thermally depositing 50 nm of Ca, venting to swap sources, and thermally depositing 100 nm of Al. Voltage-dependent EAS was performed at 420 nm wavelength.

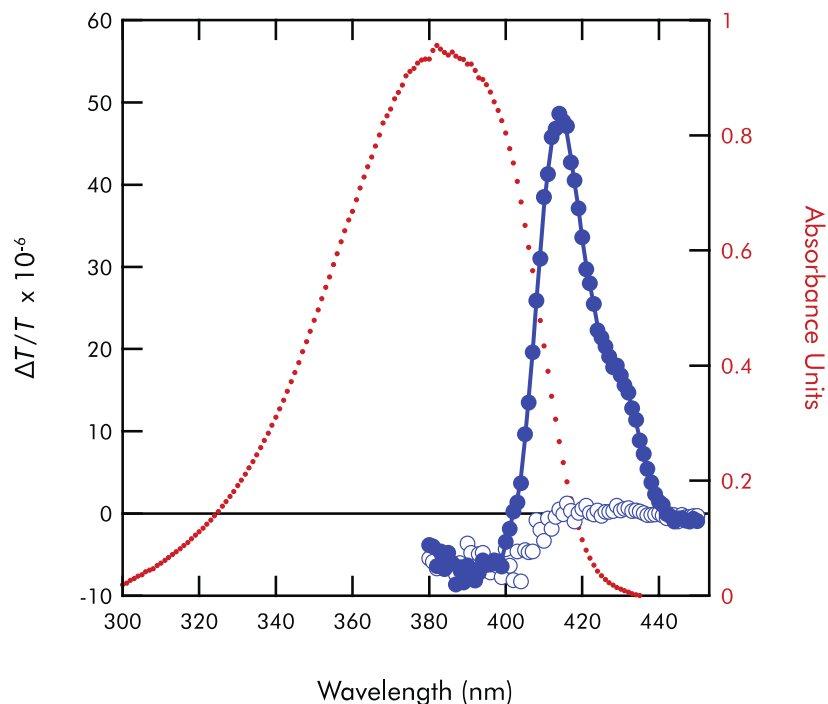


**Figure A-6:** The absorbance of a PFO film is shown in the red dots on the scale of the right axis. The electroabsorption spectrum of a diode made from the same film and of structure ITO/PFO/Al, is shown on the scale of the left axis. The blue-filled circles are the in-phase response, with line as a guide to the eye, and the blue unfilled circles are the negligible quadrature response. These electroabsorption spectra were recorded at -2 V DC, 1 V AC (peak-to-peak). Data located in group data storage at \\Bradley MacLeod\Data\BM6\BM6\_137\_x122 – EA PFO PA SAMs\.

We see for P3HT diodes that  $V_{bi}$  is independent of  $\Phi$  for the PAs used in this study which result in the smallest and largest absolute  $\Phi$ , which can be described in terms of the expected Fermi-level pinning in P3HT (Bardeen limit of operation); Tengstedt et al. observed pinning for substrate  $\Phi$  at  $\sim 4$  eV,<sup>72</sup> well above the ionization energy, which is commensurate with the lowest  $\Phi$  we measure for functionalized ITO being 4.17 eV (Table 2-1). The findings from the PFO diodes show that the sub-unity slope is not only due to the SY polymer investigated, and suggests that the nature of the ITO/SAM/polymer interface does not deviate from the Schottky-Mott limit entirely from properties pertaining to the organic. While the deposition techniques varied between these experiments and those reported in the main text, deviations from the trend lines were more likely to be due to the batch-to-batch type of variation than inherent differences in the coverage, and we expect that SAM coverage on ITO was comparable due to similarities in the process techniques (using the same batches of PAs and same supplier of ITO). These results of sub-unity  $S$  and Fermi-level pinning support the description of an ambient-processed organic-electrode interface that is unlike any previously reported.

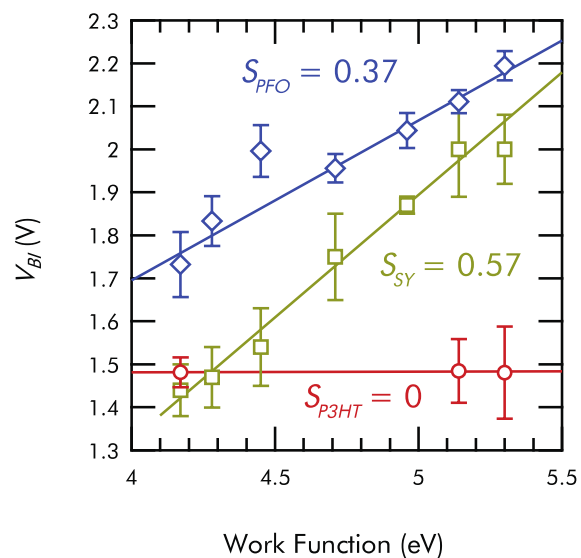


**Figure A-7:**  $V_{bi}$  for PFO (blue diamonds), SY (yellow squares), and P3HT (red circles) versus the LIXPS  $\Phi$ 's reported in Table 2-1. The lines represent linear fits excluding the third data point for PFO and the seventh data point for SY. We show the slope of these fits as 0.37 for PFO, 0.57 for SY, and 0 for P3HT. The data for SY is shown for reference, but is the same as is displayed in Figure 2-11 of the main text.

## A-5. UPS HOMO level for Super Yellow

The Schottky-Mott model for simple contacts suggest that the barrier height for charges, formed at the interface, can be directly determined from the  $\Phi$  of the contact and the ionization potential of the organic. This simple scenario assumes vacuum level alignment between the organic and the electrode and band bending from a redistribution of charge, commonly between a metal and an organic. Alternatively, in the presence of a surface dipole a vacuum level shift is observed, but is independent of the  $\Phi$  of the metal. As stated in the main text, this results in an  $S$  of unity.

In the case of TCOs, an interface with an organic is sufficiently more complex. Addition of adsorbates may alter the  $\Phi$  and local electron density at the surface and can greatly perturb the interface with low carrier concentration organics. Addition of small molecule modifiers can provide for changes in  $\Phi$  via the bond dipole with the oxide and/or the molecular dipole of the head group. Using the same attachment group with a series of different polarity head groups allows for a systematic study of the impact of surface dipoles at the interface, but results in a change in the electric field distribution within the oxide depletion layer. Therefore, it is not expected that oxides would form simple Schottky-Mott contacts.

Ultraviolet photoemission spectroscopy can be used to measure the change in both ionization energy (IE) and  $\Phi$  upon formation of an interface. We first considered the interface between ITO and the SY, as shown in Figure A-8. There is no discernible difference in vacuum level shift, as seen in the low kinetic energy/high binding energy edge. This yielded the same  $\Phi$  for both the ITO and the SY (4.1 eV). The onset of the ionization energy of SY occurs at 5.7 eV and occurs at 1.6 eV from the Fermi level.

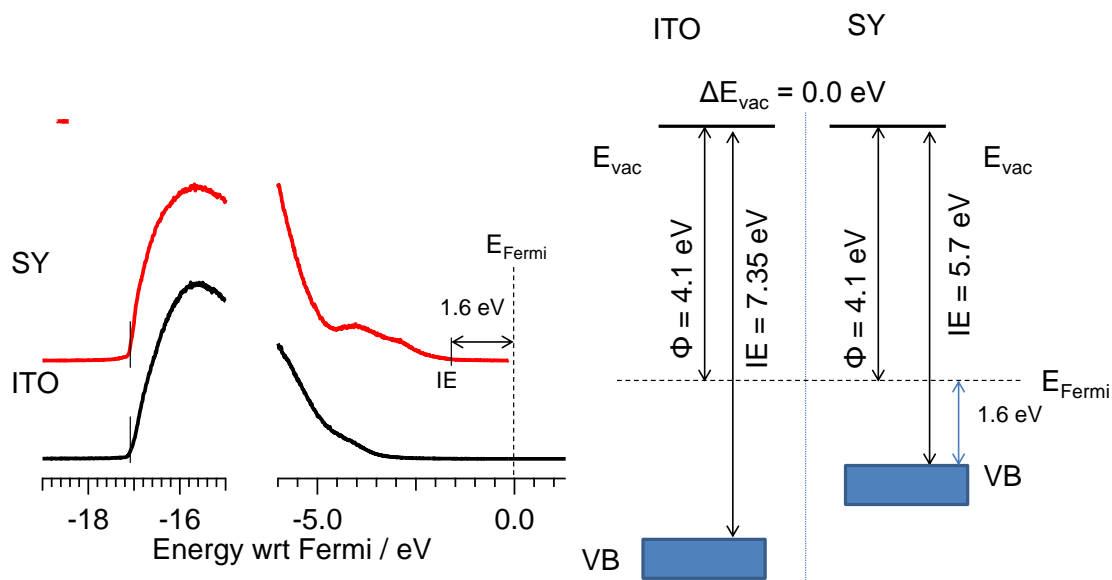


**Figure A-8: UPS and resultant energy band diagram for ITO and SY on ITO.**

An interface between a pCF<sub>3</sub>-modified ITO (PA-ITO) substrate and SY was also measured using UPS and is shown in Figure A-9. The addition of the SAM shifts the  $\Phi$  of the substrate to 4.8 eV. Addition of SY results in a dipole shift of -0.3 eV, resulting in a  $\Phi$  of 4.5 eV for the SY on PA-modified ITO. The IE of the SY is now 5.4 eV and is sufficiently closer to the Fermi level (0.9 eV), relative to SY on ITO (1.6 eV). Changes in ionization potential for  $\pi$ -conjugated systems can result from initial state effects, which imply changes in ring twisting, or final state effects, such as changes in the screening of the hole in the photoemission process. The results in Figures A-8 and A-9 indicate that there is a clear interfacial phenomenon occurring between the SY and the PA-modified ITO, and thus, this contact cannot be modeled as a simple Schottky-Mott barrier, consistent with the findings of a slope parameter not equivalent to unity.

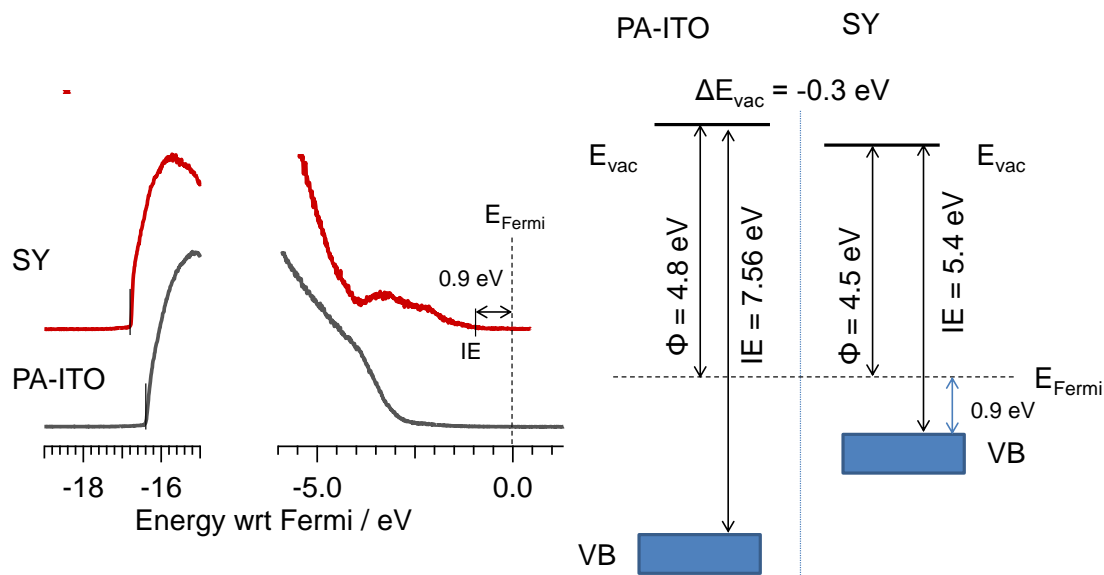


**Figure A-9: UPS and resultant energy band diagram for a PA-modified ITO substrate and subsequent interface with SY.**

We note that the  $\Phi$  of the ITO and PA-ITO substrate vary from the value obtained by LIXPS. The ITO and PA-ITO substrates were prepared at the University of Washington with procedures identical to the experimental methods of the main text, except that the incubation period was only 12 hours (rather than 48 hours). The substrates were shipped to the University of Arizona, where thin SY films ( $\sim 10$  nm) were spincoated without further treatment. These differences in SAM deposition and subsequent interface formation may contribute to the discrepancy. The error in energy measurements by UPS was given as  $\pm 0.1$  eV.

## **A-6. Post-treatment of PA SAMs with a basic solution**

A base treatment, either in the form of ultrasonication in or rinsing with 5 vol % triethylamine in ethanol, was historically implemented to remove multilayers (those exceeding a monolayer) of PA SAMs on ITO, sometimes before and sometimes after the annealing (after the deposition). Preliminary studies using the PA SAMs from the Marder group showed that when PA SAMs were deposited onto ITO by the microcontact printing method (described in Knesting et al.<sup>50</sup>), the PAs formed multilayers. Post-treating these multilayer PAs with a basic solution showed to be sufficient to reducing the PA coverage to sub-multilayer.<sup>50</sup> However, it was later found that the base treatment was probably not necessary, or beneficial, for samples prepared with a soak deposition; starting with experiment #148, batch #5 (in BM8, starting on p. 255), the procedure was no longer used for PA SAMs deposited with a soaking-type deposition procedure, rather, the warm soaking methods described in Section 2-2 were adopted.

## A-7. LIXPS beam damage studies

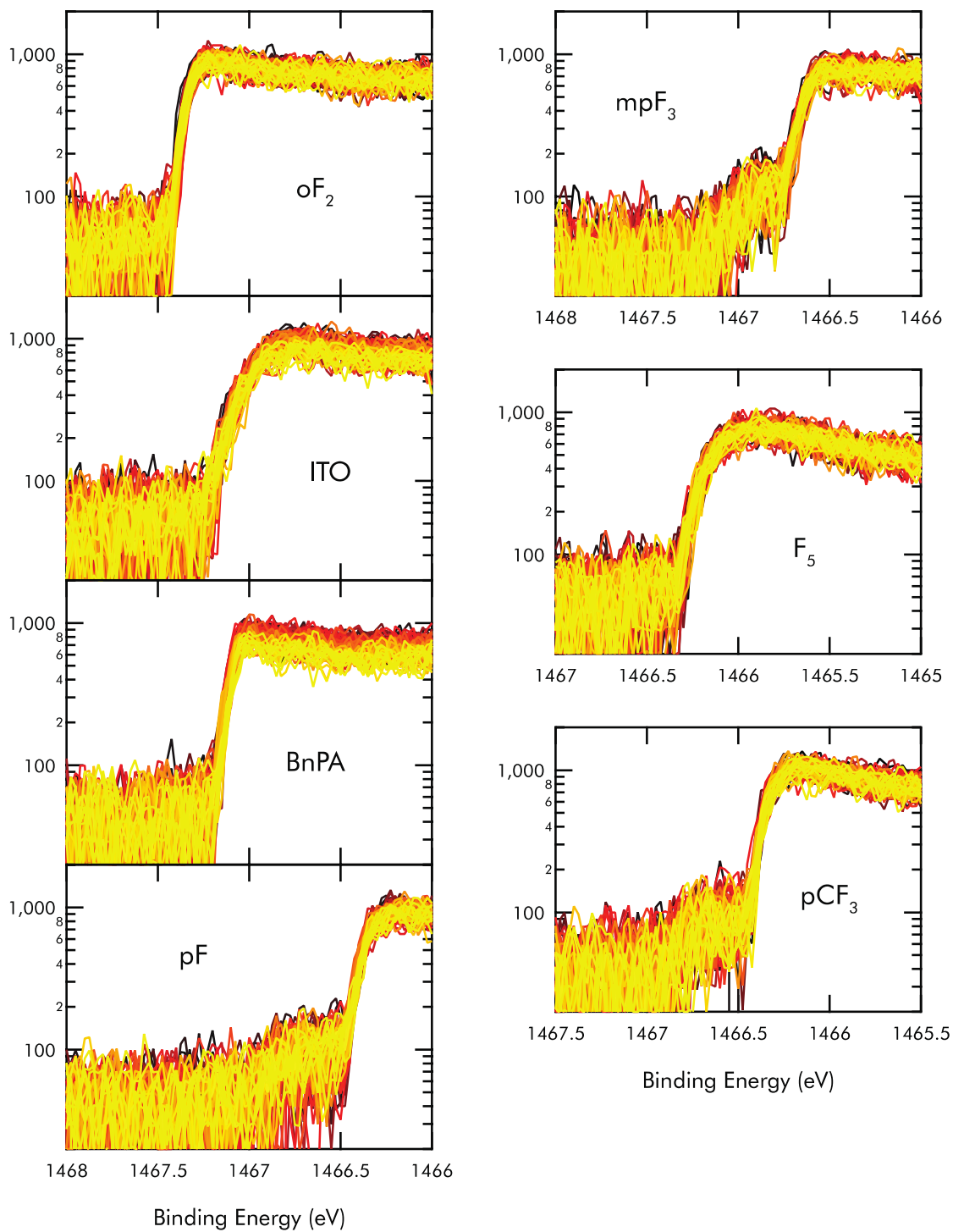


Figure A-10: Beam damage studies of the various LIXPS sample types. Data located in group data storage at \\Bradley MacLeod\Data\BM8\BM8\_083\_x154 - PA SAMs XPS & EAS\2011.10.05 XPS\.

**Table A-1: The mean and standard deviation of the SEC binding energy from 100 subsequent measurements at the same spot of each sample, with the corresponding mean  $\Phi$ .**

<b>SAM</b>	<b>BE (eV)</b>	<b><math>\Phi</math> (eV)</b>
<b>oF<sub>2</sub></b>	1467.34	4.26
<b>(ITO)</b>	1467.03	4.57
<b>BnPA</b>	1467.11	4.49
<b>mpF<sub>3</sub></b>	1466.65	4.95
<b>pF</b>	1466.37	5.23
<b>F<sub>5</sub></b>	1466.18	5.42
<b>pCF<sub>3</sub></b>	1466.35	5.25

To verify that LIXPS was not altering the sample surface during measurement, we performed the same study as was displayed in Figure 2-5, with 100 subsequent measurements being performed at the same spot, but only for the X-ray power setting in “Idle” mode. A linear regression to the measured binding energy with respect to scan number (time) showed an insignificant change ( $\ll 0.001$  eV/scan); this indicates that the LIXPS method does not alter the sample surface with the X-ray dosage required to compile statistical representation of the SEC feature. It should be noted that for some of the samples measured in this experiment, there is significant background intensity at binding energies above the main SEC feature; this pre-edge feature may be due to less surface coverage density of the PAs and/or some degree of surface contamination above or between PA molecules, which could lead to a distribution of lower kinetic energy electrons which escape the sample under X-ray illumination.<sup>57</sup> The values of  $\Phi$  obtained from these single-spot measurements vary from those used in CHAPTER 2, even though the Au standard gave a statistically indistinguishable  $\Phi$  (5.33 eV) and were not used in reporting of  $\Phi$ , due to the probability of surface contamination. This variation highlights the need for further characterization of the

deposition techniques. Although care was taken to implement the ITO functionalization using exactly the same protocol, these batch-to-batch variations seem to be common within our current techniques. One potentially large source of this variation can be in the plasma-cleaning process, which is known to produce an atmospherically unstable surface [REFS] and for which we have evidence of plasma cleaner induced contamination (See Appendix A-9).

#### **A-8. XPS survey scans**

Here we show qualitative surveys of the chemical species of interest on PA SAM functionalized ITO surfaces. Survey scans are collected with sample at 45° from normal with the detector, with no bias applied to sample, 23.6 W X-ray power, 0.025 eV step size, 50 ms dwell time, and number of samples (repeats) and pass energy indicated in the figure captions. The sample types are similar to those described in Section 2-3, but also includes an Ar-sputtered ITO for chemical referencing of an uncontaminated ITO surface. The sample preparation was slightly different though; after the incubation, the samples were rinsed with copious neat ethanol and then ultrasonicated in 5 vol % triethylamine in ethanol (discussed in Appendix 0). The sputtered ITO is emitted from Figure A-12 as there was no significant counts in the C 1s spectral region. The N 1s region was also scanned to look for residual nitrogen that may be left after implementing a triethylamine cleaning procedure, but no significant counts were observed. The data in this section was collected prior to the data in Section 2-3 or Section A-9; the question of surface contaminants was addressed in the study described in Section A-9. Data for this section is located in group data storage at \\Bradley MacLeod\Data\BM7\BM7\_142\_x147 – XPS of PA SAMs II\XPS\.

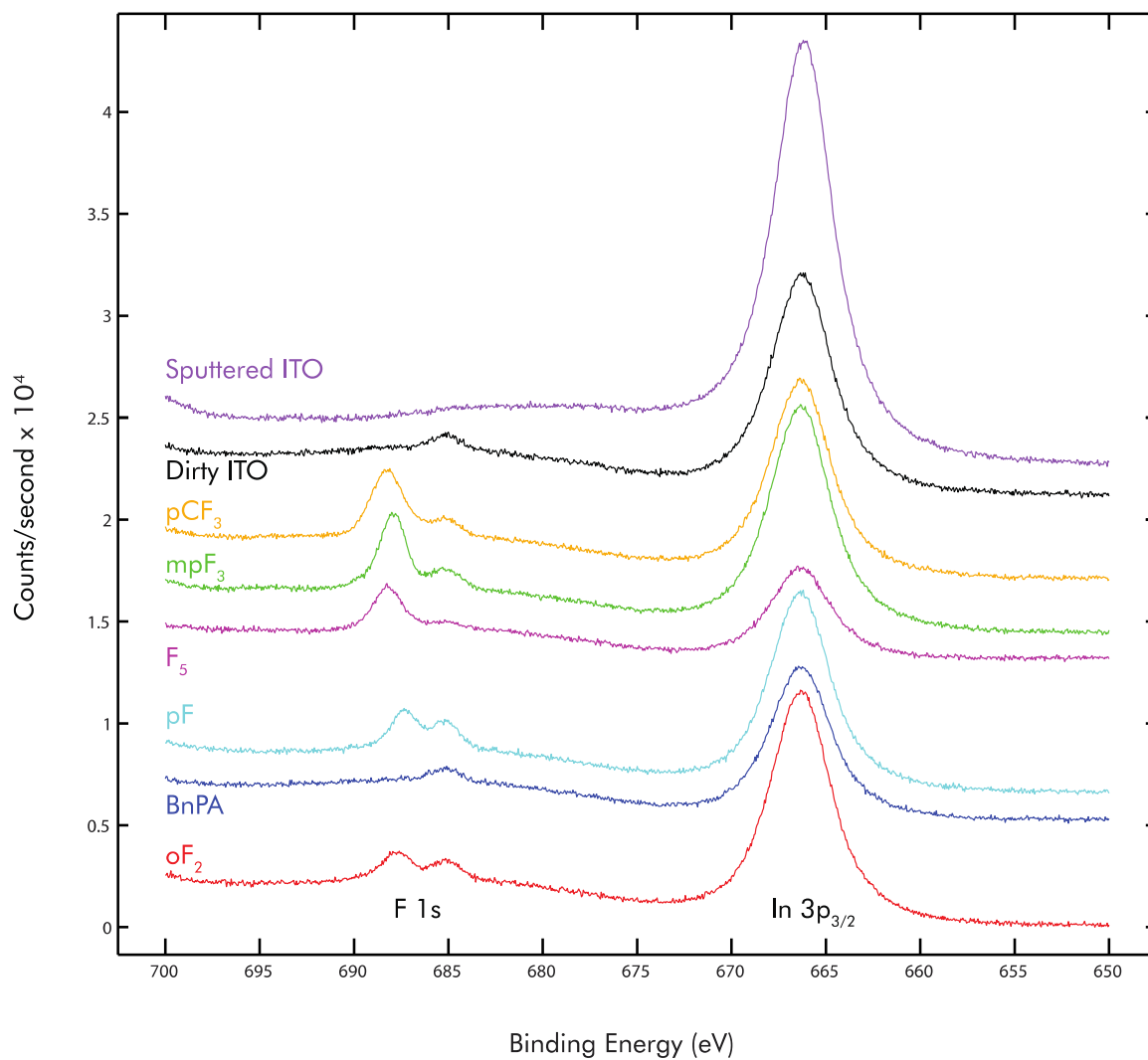


**Figure A-11: XPS Survey scan of the In 3p<sub>3/2</sub> and F 1s core regions for the XPS samples; 50 repeats at 46.95 eV pass energy.**

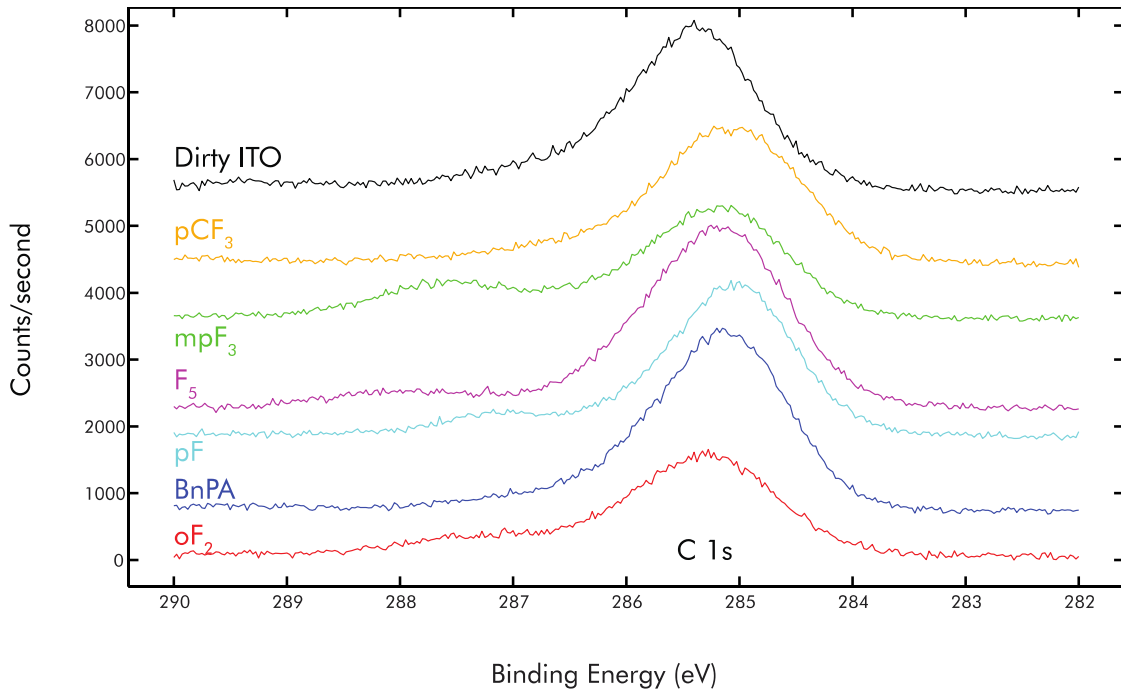


Figure A-12: XPS Survey scan of the C 1s core regions for the XPS samples; 30 repeats at 23.5 eV pass energy.

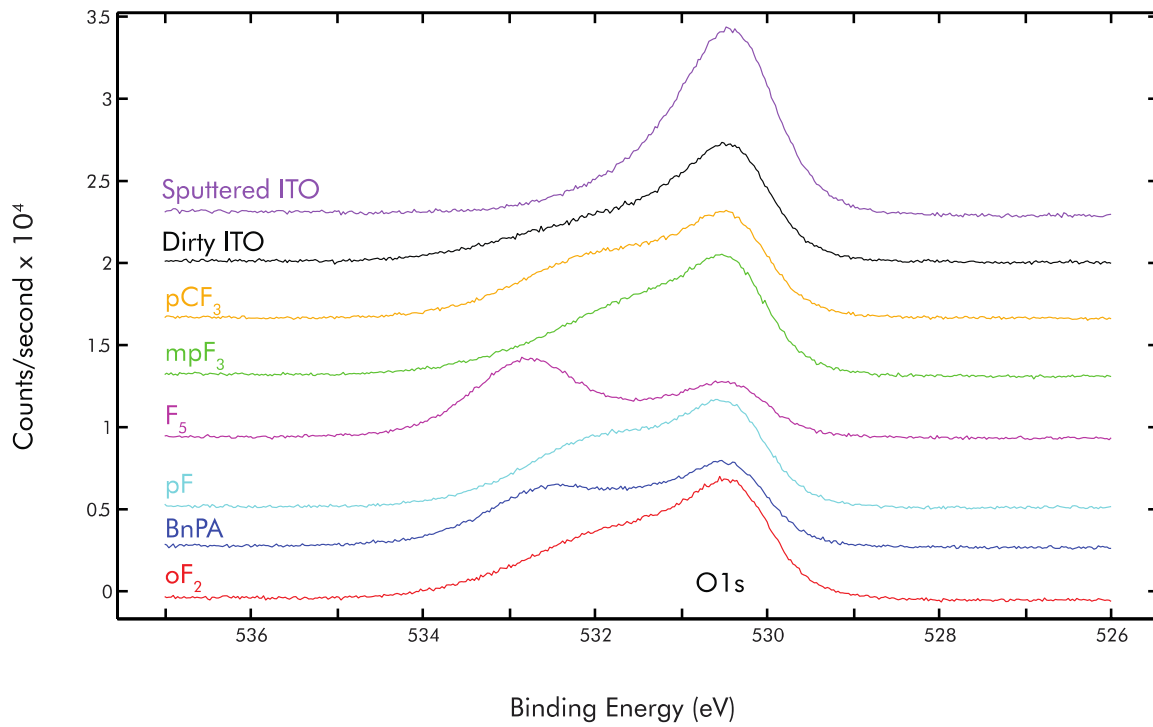
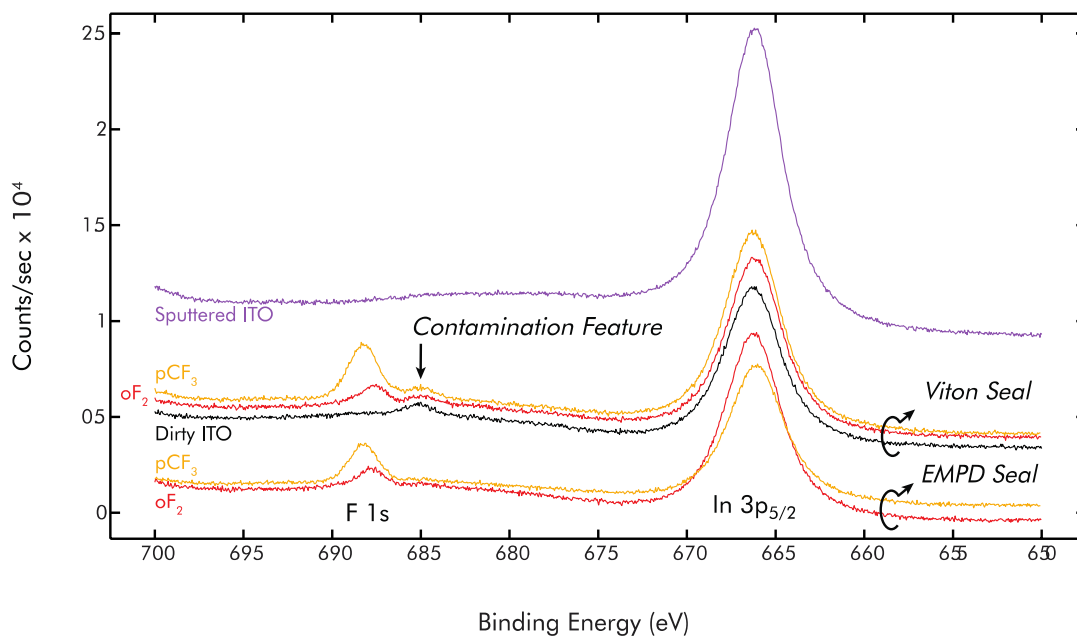


Figure A-13: XPS Survey scan of the O 1s core regions for the XPS samples; 40 repeats at 23.5 eV pass energy.

## A-9. Plasma cleaner-induced contamination identified with XPS

Functionalization of ITO surfaces with the phosphonic acids (PAs) appears to be quite sensitive to the ITO preparation (detergent and solvent cleaning), the oxygen plasma activation, and subsequent ambient exposures, and great care was taken in order to achieve reproducible coverage. It has previously been advised that care should be taken when plasma cleaning such that further surface contaminants are not deposited to the sample during the plasma process.<sup>100</sup> In the Harrick PDC-32G plasma cleaner, a plasticized rubber O-ring creates the vacuum seal between the anodized aluminum lid and the glass chamber (either borosilicate or Pyrex); this O-ring is exposed to the volume of the chamber in which the plasma is created. Evidence of O-ring contamination was observed by X-ray photoelectron spectroscopy. Figure A-14 shows XPS two different PA monolayers on ITO fabricated identically from the same two PA solutions, but with the O-ring being switched from a Viton O-ring to an ethylene propylene diene monomer (EPDM) rubber O-ring. A feature at ~685 eV associated with the F 1s electrons in the SAM/ITO samples is significantly reduced after the swap. Viton is polymerized from, among other things, vinylfluoride, hexylfluoropropylene, and tetrafluoroethylene – all compounds containing non-aromatic-bonded fluorine. The fluorine contained in the PAs are bonded to aromatic carbon and may there have a significantly shifted F 1s binding energy. With the differences in the carbon bonding order for fluorine atoms in the PA SAMs and those we might expect from the Viton polymerization compounds, we attribute this reduction in the lower-energy feature to elimination of the Viton-sourced surface contamination of PA SAM-on-ITO samples. Samples of poly(3,4-ethylenedioxythiophene):poly(styrenesulfonate) (PEDT:PSS) that were deposited onto substrates that were plasma cleaned in this chamber were shown with time-of-

flight secondary ion mass spectroscopy to exhibit spectral signatures of polydimethylsiloxane (PDMS). The presence of PDMS was not expected for a PEDT:PSS film and was attributed to a binding agent in a brand of lint-free cloth that had been used to clean the plasma chamber. Cleaning the plasma chamber with a Kimwipes towel and hexanes was shown to eliminate the PDMS surface contamination. The evidence for surface contamination originating from the plasma cleaner itself suggests possible sources of batch-to-batch or group-group<sup>48,49</sup> variations in observed coverage. Further, the SAM-assembly process will probably require significant controls in future systematic studies, to ensure that assumed assemblies are achieved and reproducible within the general methods outlined in Section 2-2.



**Figure A-14:** XPS spectra of two PA SAMs on ITO (pCF<sub>3</sub> in orange and oF<sub>2</sub> in red) from identically-prepared batches but changing the material of the O-ring used to seal the oxygen plasma chamber. The small feature at ~685 eV binding energy decreases when switching to an un-fluorinated O-ring material. The same feature is also removed from the ITO control (black) upon sputtering with Ar (purple). Spectra are offset for clarity. Data located in group data storage at \\Bradley MacLeod\Data\BM8\BM8\_083\_x154 – PA SAMs XPS & EAS\2011.10.05 XPS\.

## A-10. Vacuum-Referenced Energy Levels

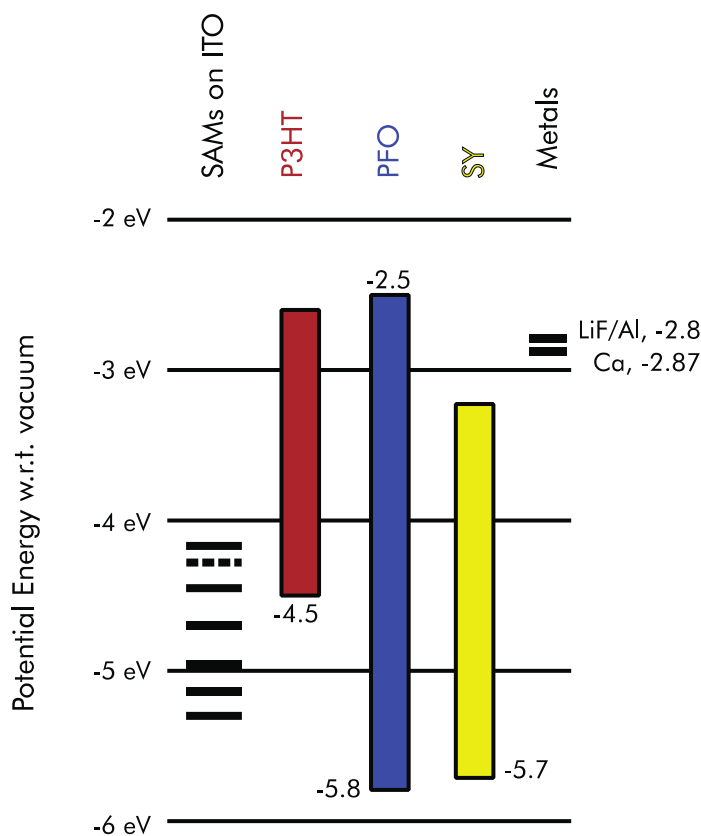


Figure A-15: Energy levels of materials in the device studies, including the work functions of ITO/SAM, HOMO and LUMO levels of polymers, and work functions of top metal contacts.

Figure A-15 is included for the visualization purposes of vacuum-referenced energy levels between the different materials used in the electroabsorption studies. The LIXPS-measured phosphonic acid SAM work functions were measured with LIXPS (Section 2-3) and are also tabulated (Table 2-1) and listed with the SAM molecules (Figure 2-3). The ionization potential for P3HT<sup>72</sup>, the ionization potential for PFO<sup>72,101</sup> and the electron affinity of PFO<sup>101</sup> are taken from literature reports. The ionization potential was measured with UPS (Appendix A-5). The work function for Ca was taken from literature.<sup>102</sup> The work function for the LiF/Al was estimated from literature.<sup>103</sup>

## BIBLIOGRAPHY

- (1) Krebs, F. C. *Sol. Energy Mater. Sol. Cells* **2009**, *93*, 394–412.
- (2) Jørgensen, M.; Norrman, K.; Krebs, F. C. *Sol. Energy Mater. Sol. Cells* **2008**, *92*, 686–714.
- (3) Krebs, F. C.; Carlé, J. E.; Cruys-Bagger, N.; Andersen, M.; Lilliedal, M. R.; Hammond, M. A.; Hvidt, S. *Sol. Energy Mater. Sol. Cells* **2005**, *86*, 499–516.
- (4) Kim, N.; Potscavage, W. J.; Domercq, B.; Kippelen, B.; Graham, S. *Appl. Phys. Lett.* **2009**, *94*, 163308–163308–3.
- (5) Forrest, S. R. *MRS Bull.* **2005**, *30*, 28–32.
- (6) Spanggaard, H.; Krebs, F. C. *Sol. Energy Mater. Sol. Cells* **2004**, *83*, 125–146.
- (7) Deibel, C.; Dyakonov, V. *Rep. Prog. Phys.* **2010**, *73*, 096401.
- (8) Sariciftci, N. S.; Smilowitz, L.; Heeger, A. J.; Wudl, F. *Science* **1992**, *258*, 1474–1476.
- (9) Png, R.-Q.; Chia, P.-J.; Sivaramakrishnan, S.; Wong, L.-Y.; Zhou, M.; Chua, L.-L.; Ho, P. K. H. *Appl. Phys. Lett.* **2007**, *91*, 013511–3.
- (10) Chia, P. J.; Chua, L. L.; Sivaramakrishnan, S.; Zhuo, J. M.; Zhao, L. H.; Sim, W. S.; Yeo, Y. C.; Ho, P.; others *Adv. Mater.* **2007**, *19*, 4202–4207.
- (11) Pettersson, L. A. A.; Roman, L. S.; Inganäs, O. *J. Appl. Phys.* **1999**, *86*, 487–496.
- (12) Hummelen, J. C.; Knight, B. W.; LePeq, F.; Wudl, F.; Yao, J.; Wilkins, C. L. *J. Org. Chem.* **1995**, *60*, 532–538.
- (13) Shaheen, S. E.; Brabec, C. J.; Sariciftci, N. S.; Padinger, F.; Fromherz, T.; Hummelen, J. C. *Appl. Phys. Lett.* **2001**, *78*, 841–843.
- (14) Green, M. A.; Emery, K.; Hishikawa, Y.; Warta, W.; Dunlop, E. D. *Prog. Photovolt: Res. Appl* **2012**, *20*, 12–20.
- (15) Cates, N. C.; Gysel, R.; Dahl, J. E. P.; Sellinger, A.; McGehee, M. D. *Chem. Mater.* **2010**, *22*, 3543–3548.
- (16) Giridharagopal, R.; Ginger, D. S. *J. Phys. Chem. Lett.* **2010**, *1*, 1160–1169.
- (17) Giridharagopal, R.; Shao, G.; Groves, C.; Ginger, D. S. *Mater. Today* **2010**, *13*, 50–56.
- (18) Reid, O. Scanning probe microscopy of organic solar cells, University of Washington: Seattle, WA, 2010.
- (19) Coffey, D. C.; Reid, O. G.; Rodovsky, D. B.; Bartholomew, G. P.; Ginger, D. S. *Nano Lett.* **2007**, *7*, 738–744.
- (20) Germack, D. S.; Chan, C. K.; Kline, R. J.; Fischer, D. A.; Gundlach, D. J.; Toney, M. F.; Richter, L. J.; DeLongchamp, D. M. *Macromolecules* **2010**, *43*, 3828–3836.
- (21) Wang, D. H.; Kim, D. Y.; Choi, K. W.; Seo, J. H.; Im, S. H.; Park, J. H.; Park, O. O.; Heeger, A. J. *Angew. Chem., Int. Ed.* **2011**, *50*, 5519–5523.
- (22) Tillack, A. F.; Noone, K. M.; MacLeod, B. A.; Nordlund, D.; Nagle, K. P.; Bradley, J. A.; Hau, S. K.; Yip, H.-L.; Jen, A. K.-Y.; Seidler, G. T.; Ginger, D. S. *ACS Appl. Mater. Interfaces* **2011**, *3*, 726–732.
- (23) Manceau, M.; Rivaton, A.; Gardette, J.-L.; Guillerez, S.; Lemaître, N. *Polym. Degrad. Stab.* **2009**, *94*, 898–907.
- (24) Chen, L.; Hong, Z.; Li, G.; Yang, Y. *Adv. Mater.* **2009**, *21*, 1434–1449.
- (25) Li, G.; Chu, C.-W.; Shrotriya, V.; Huang, J.; Yang, Y. *Applied Physics Letters* **2006**, *88*, 253503–253503–3.

- (26) White, M. S.; Olson, D. C.; Shaheen, S. E.; Kopidakis, N.; Ginley, D. S. *Appl. Phys. Lett.* **2006**, *89*, 143517–143517–3.
- (27) Hau, S. K.; Yip, H.-L.; Ma, H.; Jen, A. K.-Y. *Appl. Phys. Lett.* **2008**, *93*, 233304–3.
- (28) Olson, D. C.; Lee, Y.-J.; White, M. S.; Kopidakis, N.; Shaheen, S. E.; Ginley, D. S.; Voigt, J. A.; Hsu, J. W. P. *J. Phys. Chem. C* **2008**, *112*, 9544–9547.
- (29) Riede, M.; Uhrich, C.; Widmer, J.; Timmreck, R.; Wynands, D.; Schwartz, G.; Gnehr, W.; Hildebrandt, D.; Weiss, A.; Hwang, J.; Sundarraj, S.; Erk, P.; Pfeiffer, M.; Leo, K. *Adv. Funct. Mater.* **2011**, *21*, 3019–3028.
- (30) Andersson, L. M.; Müller, C.; Badada, B. H.; Zhang, F.; Würfel, U.; Inganäs, O. *J. Appl. Phys.* **2011**, *110*, 024509.
- (31) Lee, J.; Vandewal, K.; Yost, S. R.; Bahlke, M. E.; Goris, L.; Baldo, M. A.; Manca, J. V.; Voorhis, T. V. *J. Am. Chem. Soc.* **2010**.
- (32) Pal, S. K.; Kesti, T.; Maiti, M.; Zhang, F.; Inganäs, O.; Hellström, S.; Andersson, M. R.; Oswald, F.; Langa, F.; Österman, T.; others *Journal of the American Chemical Society* **2010**.
- (33) Howard, I. A.; Mauer, R.; Meister, M.; Laquai, F. *J. Am. Chem. Soc.* **2010**, *132*, 14866–14876.
- (34) Giebink, N. C.; Lassiter, B. E.; Wiederrecht, G. P.; Wasielewski, M. R.; Forrest, S. R. *Phys. Rev. B* **2010**, *82*, 155306.
- (35) Müller, J.; Lupton, J.; Feldmann, J.; Lemmer, U.; Scharber, M.; Sariciftci, N.; Brabec, C.; Scherf, U. *Phys. Rev. B* **2005**, *72*, 195208.
- (36) Offermans, T.; van Hal, P.; Meskers, S.; Koetse, M.; Janssen, R. *Phys. Rev. B* **2005**, *72*, 045213.
- (37) Peumans, P.; Forrest, S. R. *Chem. Phys. Lett.* **2004**, *398*, 27–31.
- (38) Mihailetschi, V. D.; Koster, L. J. A.; Hummelen, J. C.; Blom, P. W. M. *Phys. Rev. Lett.* **2004**, *93*, 216601.
- (39) Ramsdale, C. M.; Barker, J. A.; Arias, A. C.; MacKenzie, J. D.; Friend, R. H.; Greenham, N. C. *J. Appl. Phys.* **2002**, *92*, 4266–4270.
- (40) Koster, L. J. A.; Smits, E. C. P.; Mihailetschi, V. D.; Blom, P. W. M. *Phys. Rev. B* **2005**, *72*, 085205.
- (41) Mozer, A.; Dennler, G.; Sariciftci, N.; Westerling, M.; Pivrikas, A.; Österbacka, R.; Juška, G. *Phys. Rev. B* **2005**, *72*, 035217.
- (42) Zimmermann, B.; Glatthaar, M.; Niggemann, M.; Riede, M.; Hinsch, A. *Thin Solid Films* **2005**, *493*, 170–174.
- (43) Hwang, J.; Wan, A.; Kahn, A. *Mater. Sci. Eng., R* **2009**, *64*, 1–31.
- (44) Campbell, I. H.; Rubin, S.; Zawodzinski, T. A.; Kress, J. D.; Martin, R. L.; Smith, D. L.; Barashkov, N. N.; Ferraris, J. P. *Phys. Rev. B* **1996**, *54*, R14321–R14324.
- (45) Brown, T. M.; Friend, R. H.; Millard, I. S.; Lacey, D. J.; Burroughes, J. H.; Cacialli, F. *Appl. Phys. Lett.* **2000**, *77*, 3096–3098.
- (46) Brown, T. M.; Friend, R. H.; Millard, I. S.; Lacey, D. J.; Butler, T.; Burroughes, J. H.; Cacialli, F. *J. Appl. Phys.* **2003**, *93*, 6159–6172.
- (47) Hoven, C. V.; Peet, J.; Mikhailovsky, A.; Nguyen, T. Q. *Appl. Phys. Lett.* **2009**, *94*, 033301.
- (48) Hotchkiss, P. J.; Li, H.; Paramonov, P. B.; Paniagua, S. A.; Jones, S. C.; Armstrong, N. R.; Brédas, J.-L.; Marder, S. R. *Adv. Mater.* **2009**, *21*, 4496–4501.

- (49) Sharma, A.; Hotchkiss, P. J.; Marder, S. R.; Kippelen, B. *J. Appl. Phys.* **2009**, *105*, 084507.
- (50) Knesting, K. M.; Hotchkiss, P. J.; MacLeod, B. A.; Marder, S. R.; Ginger, D. S. *Adv. Mater.* **2012**, *24*, 642–646.
- (51) Campbell, I. H.; Kress, J. D.; Martin, R. L.; Smith, D. L.; Barashkov, N. N.; Ferraris, J. P. *Appl. Phys. Lett.* **1997**, *71*, 3528–3530.
- (52) Hotchkiss, P. J. The design, synthesis, and use of phosphonic acids for the surface modification of metal oxides, Georgia Institute of Technology: Atlanta, GA, 2008.
- (53) Edman, L.; Summers, M. A.; Buratto, S. K.; Heeger, A. J. *Phys. Rev. B* **2004**, *70*, 115212.
- (54) Spreitzer, H.; Becker, H.; Kluge, E.; Kreuder, W.; Schenk, H.; Demandt, R.; Schoo, H. *Adv. Mater.* **1998**, *10*, 1340–1343.
- (55) Yi, Y.; Lyon, J. E.; Beerbom, M. M.; Schlaf, R. *J. Appl. Phys.* **2006**, *100*, 093719.
- (56) Beerbom, M. M.; Lägél, B.; Cascio, A. J.; Doran, B. V.; Schlaf, R. *J. Electron Spectrosc. Relat. Phenom.* **2006**, *152*, 12–17.
- (57) Helander, M. G.; Greiner, M. T.; Wang, Z. B.; Lu, Z. H. *Appl. Surf. Sci.* **2010**, *256*, 2602–2605.
- (58) Helander, M. G.; Greiner, M. T.; Wang, Z. B.; Tang, W. M.; Lu, Z. H. *J. Vac. Sci. Technol., A* **2011**, *29*, 011019.
- (59) Schlaf, R.; Murata, H.; Kafafi, Z. H. *J. Electron Spectrosc. Relat. Phenom.* **2001**, *120*, 149–154.
- (60) Seah, M. P. *Surf. Interface Anal.* **2001**, *31*, 721–723.
- (61) Park, Y.; Choong, V.; Gao, Y.; Hsieh, B. R.; Tang, C. W. *Appl. Phys. Lett.* **1996**, *68*, 2699–2701.
- (62) Ertl, G. *Low energy electrons and surface chemistry*; Verlag Chemie: Weinheim, 1974.
- (63) Worland, R. S. *Electroabsorption in Conjugated Polymers*, University of California, Santa Barbara., 1989.
- (64) Wieser, G.; Horváth, Á. In *Primary Photoexcitations in Conjugated Polymers: Molecular Exciton versus Semiconductor Band Model*; World Scientific Publ.: Singapore, 1997.
- (65) Jalviste, E.; Ohta, N. *J. Photochem. Photobiol., C* **2007**, *8*, 30–46.
- (66) Brown, T. M.; Kim, J. S.; Friend, R. H.; Cacialli, F.; Daik, R.; Feast, W. J. *Appl. Phys. Lett.* **1999**, *75*, 1679–1681.
- (67) Bodrozic, V.; Roberts, M.; Phillips, N.; Burroughes, J. H.; Mian, S.; Cacialli, F. *J. Appl. Phys.* **2007**, *101*, 084507.
- (68) Brown, T. M.; Cacialli, F. In *Conjugated Polymers: Theory, Synthesis, Properties, and Characterization*; Skotheim, T. A.; Reynolds, J. R., Eds.; CRC Press, 2007.
- (69) Harrison, M. G.; Möller, S.; Weiser, G.; Urbasch, G.; Mahrt, R. F.; Bäessler, H.; Scherf, U. *Phys. Rev. B* **1999**, *60*, 8650–8658.
- (70) Horváth, Á.; Bäessler, H.; Weiser, G. *Phys. Status Solidi B* **1992**, *173*, 755–764.
- (71) Horváth, Á.; Weiser, G.; Baker, G. L.; Etemad, S. *Phys. Rev. B* **1995**, *51*, 2751–2758.
- (72) Tengstedt, C.; Osikowicz, W.; Salaneck, W. R.; Parker, I. D.; Hsu, C.-H.; Fahlman, M. *Appl. Phys. Lett.* **2006**, *88*, 053502.
- (73) Blakesley, J. C.; Greenham, N. C. *J. Appl. Phys.* **2009**, *106*, 034507.
- (74) Mönch, W. *Rep. Prog. Phys.* **1990**, *53*, 221–278.
- (75) Mönch, W. *Surf. Sci.* **1994**, *299-300*, 928–944.
- (76) Vázquez, H.; Flores, F.; Kahn, A. *Org. Electron.* **2007**, *8*, 241–248.
- (77) Li, H.; Paramonov, P.; Bredas, J.-L. *J. Mater. Chem.* **2010**, *20*, 2630–2637.

- (78) Pillai, S.; Catchpole, K. R.; Trupke, T.; Zhang, G.; Zhao, J.; Green, M. A. *Appl. Phys. Lett.* **2006**, *88*, 161102.
- (79) Cubukcu, E.; Kort, E. A.; Crozier, K. B.; Capasso, F. *Appl. Phys. Lett.* **2006**, *89*, 093120.
- (80) Pillai, S.; Catchpole, K. R.; Trupke, T.; Green, M. A. *J. Appl. Phys.* **2007**, *101*, 093105.
- (81) Mayer, K. M.; Hafner, J. H. *Chem. Rev.* **2011**, *111*, 3828–3857.
- (82) Maier, S. A. *Plasmonics: Fundamentals and Applications*; 2007.
- (83) Atwater, H. A.; Polman, A. *Nat. Mater.* **2010**, *9*, 205–213.
- (84) Chen, F.-C.; Wu, J.-L.; Lee, C.-L.; Hong, Y.; Kuo, C.-H.; Huang, M. H. *Appl. Phys. Lett.* **2009**, *95*, 013305.
- (85) Kim, K.; Carroll, D. L. *Appl. Phys. Lett.* **2005**, *87*, 203113.
- (86) Kim, S.-S.; Na, S.-I.; Jo, J.; Kim, D.-Y.; Nah, Y.-C. *Appl. Phys. Lett.* **2008**, *93*, 073307.
- (87) Lee, J. H.; Park, J. H.; Kim, J. S.; Lee, D. Y.; Cho, K. *Org. Electron.* **2009**, *10*, 416–420.
- (88) Morfa, A. J.; Rowlen, K. L.; Reilly, T. H.; Romero, M. J.; van de Lagemaat, J. *Appl. Phys. Lett.* **2008**, *92*, 013504.
- (89) Rand, B. P.; Peumans, P.; Forrest, S. R. *J. Appl. Phys.* **2004**, *96*, 7519.
- (90) Wu, J.-L.; Chen, F.-C.; Hsiao, Y.-S.; Chien, F.-C.; Chen, P.; Kuo, C.-H.; Huang, M. H.; Hsu, C.-S. *ACS Nano* **2011**, *5*, 959–967.
- (91) Xue, M.; Li, L.; Tremolet de Villers, B. J.; Shen, H.; Zhu, J.; Yu, Z.; Stieg, A. Z.; Pei, Q.; Schwartz, B. J.; Wang, K. L. *Appl. Phys. Lett.* **2011**, *98*, 253302.
- (92) Yang, J.; You, J.; Chen, C.-C.; Hsu, W.-C.; Tan, H.; Zhang, X. W.; Hong, Z.; Yang, Y. *ACS Nano* **2011**, *5*, 6210–6217.
- (93) Topp, K.; Borchert, H.; Johnen, F.; Tunc, A. V.; Knipper, M.; von Hauff, E.; Parisi, J.; Al-Shamery, K. *J. Phys. Chem. A* **2010**, *114*, 3981–3989.
- (94) Stavtyska-Barba, M.; Kelley, A. M. *J. Phys. Chem. C* **2010**, *114*, 6822–6830.
- (95) Kulkarni, A. P.; Noone, K. M.; Munechika, K.; Guyer, S. R.; Ginger, D. S. *Nano Lett.* **2010**, *10*, 1501–1505.
- (96) Paniagua, S. A.; Hotchkiss, P. J.; Jones, S. C.; Marder, S. R.; Mudalige, A.; Marrikar, F. S.; Pemberton, J. E.; Armstrong, N. R. *J. Phys. Chem. C* **2008**, *112*, 7809–7817.
- (97) Sharma, A.; Kippelen, B.; Hotchkiss, P. J.; Marder, S. R. *Appl. Phys. Lett.* **2008**, *93*, 163308–3.
- (98) Sharma, A.; Haldi, A.; Potscavage Jr., W. J.; Hotchkiss, P. J.; Marder, S. R.; Kippelen, B. *J. Mater. Chem.* **2009**, *19*, 5298–5302.
- (99) Sharma, A.; Haldi, A.; Hotchkiss, P. J.; Marder, S. R.; Kippelen, B. *J. Appl. Phys.* **2009**, *105*, 074511.
- (100) Synowicki, R. A. *J. Vac. Sci. Technol., A* **1996**, *14*, 3075.
- (101) Hwang, J.; Kim, E.-G.; Liu, J.; Brédas, J.-L.; Duggal, A.; Kahn, A. *J. Phys. Chem. C* **2007**, *111*, 1378–1384.
- (102) Michaelson, H. B. *J. Appl. Phys.* **1977**, *48*, 4729–4733.
- (103) Shaheen, S. E.; Jabbour, G. E.; Morrell, M. M.; Kawabe, Y.; Kippelen, B.; Peyghambarian, N.; Nabor, M.-F.; Schlaf, R.; Mash, E. A.; Armstrong, N. R. *J. Appl. Phys.* **1998**, *84*, 2324.

# CURRICULUM VITAE

---

## EDUCATION

---

- Ph.D., Materials Chemistry  
University of Washington, Seattle, March 9, 2012.  
Advisor: Prof. David. S. Ginger
- B.S., Electrical Engineering, Cum Laude  
University of Alaska, Fairbanks, May 2005.

---

## RESEARCH INTERESTS

---

- Physics of hybrid/organic photovoltaic devices and their interfaces
- Other solar, renewable, and “smart” energy technologies

---

## RESEARCH EXPERIENCE

---

- I found correlation of work function (measured with low-intensity x-ray photoelectron spectroscopy and scanning Kelvin probe atomic force microscopy) with built-in potential (measured with electroabsorption spectroscopy) for self-assembling monolayer (SAM) modified indium tin oxide (ITO) electrodes used in organic photodiodes.
- We verified that spectral bleaching of silver nanoprisms was due to electron charging from the electron acceptor of a bulk heterojunction organic solar cell using charge modulation spectroscopy. If nanoprisms would be used for their previously discovered absorption enhancement effects, they would require electrical insulation from the semiconductor dyes.
- I built the electroabsorption and charge modulation spectroscopy experiments, interfacing the electronics components with custom LabVIEW code, and custom-machined parts for translating the optical cryostat.
- We revealed the molecular orientation of SAM molecules on metal-oxide substrates using angle-resolved near-edge X-ray absorption fine structure at the Stanford Synchrotron Radiation Lighthouse, Stanford Linear Accelerator Laboratory.

---

## SELECTED AWARDS

---

National Science Foundation Graduate Research Fellowship, 2007-2010.  
Carl Storm Underrepresented Minority Fellowship, 2008.  
Graduation with Leadership Honors, 2005.  
A.T. Anderson Memorial Scholarship, 2004.  
University of Alaska Scholars Award, four-year tuition credit, 1999.

---

## EMPLOYMENT

---

- Postdoctoral Researcher of Contacts and Interfaces in Organic Solar Cells, **National Renewable Energy Laboratory**, Golden, CO, starting March 2012.
- Research Assistant and NSF Fellow in physical/materials chemistry, **University of Washington**, Seattle, WA, 2006-2012.
- Engineering Intern, **NANA/Colt Engineering, LLC**, Professional Engineer's Assistant with primary responsibility of design review. Anchorage, AK, Spring 2006.
- Failure Analysis Engineer, **International Business Machines Corporation**, determination of the causes of product failures through visual inspection and base level coding. Rochester, MN, Summer 2004.
- Engineering Specialist, **Siemens Building Technologies, Inc.**, Project Engineer for a \$50k heating and ventilation controls project. Fairbanks, AK, May 2003- Apr 2004.
- Intern and Professional Engineer's Assistant, **State of Alaska, Department of Transportation**, performed research for construction proposal on Alaska's first highway interchange roundabout. Anchorage, AK, May 2002- Jan 2003.
- Intern, **VECO Alaska, Inc.**, Electrical Safety Inspections Team. Anchorage and Prudhoe Bay, AK, Summer 2001.

---

## PEER-REVIEWED PUBLICATIONS

---

- **Bradley A. MacLeod**, Noah E. Horwitz, Erin L. Ratcliff, Judith L. Jenkins, Neal R. Armstrong, Anthony J. Giordano, Peter J. Hotchkiss, Seth R. Marder, Charles T. Campbell, David S. Ginger. Built-in Potential in Conjugated Polymer Diodes with Changing Anode Work Function: Interfacial States and Deviation from the Schottky-Mott Limit. (Submitted to *J. Phys. Chem. Lett.*)
- Michael Salvador, **Bradley A. MacLeod**, Angela Hess, Abhishek P. Kulkarni and David S. Ginger. Photoinduced electron transfer to plasmonic nanoparticles in BHJ blends. (In preparation)
- Matthew Gliboff, Matthew Schalnaf, Kristina M. Knesting, Lingzi Sang, Hong Li, **Bradley A. MacLeod**, Dennis Nordlund, Anthony Giordano, Gerald T. Seidler, Jean-Luc Brédas, Seth R. Marder, Jeanne E. Pemberton, David S. Ginger. Molecular orientation of phosphonic acid interface modifiers on transparent conducting oxides. (In preparation)
- Kristina M. Knesting, Peter J. Hotchkiss, **Bradley A. MacLeod**, Seth R. Marder, David S. Ginger. Spatially modulating interfacial properties of transparent conductive oxides: patterning work function with phosphonic acid SAMs, published online in *Adv. Mater.* **2012**, *24*, 642–646.
- Andreas F. Tillack, Kevin M. Noone, **Bradley A. MacLeod**, Dennis Nordlund, Kenneth P. Nagle, Joseph A. Bradley, Steven K. Hau, Alex K.-Y. Jen, Gerald T. Seidler, David S. Ginger. Surface characterization of polythiophene:fullerene blends on different electrodes using near edge X-ray absorption fine structure, *ACS Appl. Mater. Interfaces* **2011**, *3*, 726-732.
- Liam S. C. Pingree, **Bradley A. MacLeod**, David S. Ginger, The changing face of PEDOT : PSS films: Substrate, bias, and processing effects on vertical charge transport, *J. Phys. Chem. C*, **2008**, *112*, 21, 7922-7927.

---

## EDUCATION AND OUTREACH

---

- Pacific Science Center Science Communication Fellow: Developed hands-on plastic solar cell activity: *The electron slide: Making electricity from plastics?*

- Research mentoring for honors undergraduate chemistry student, 2008 – 2011.
- Administration of a hands-on learning module in biodiesel synthesis for high schools, March 2010.
- Development of online educational material, including video demonstration, for measurement of external quantum efficiencies in photovoltaic cells, January 2010. ([bit.ly/sVxxXP](http://bit.ly/sVxxXP))
- Co-Director, web administrator, blogger, and book club organizer of The Forum on Science Ethics and Policy ([seattle.fosep.org](http://seattle.fosep.org))

---

## PRESENTATIONS

---

- Poster: "Probing nanometer-scale energetics and orientation of molecules at interfaces," U.S. DOE EFRC Summit, Washington D.C., May 2011.
- Talk: "Electroabsorption spectroscopy: Finding your built-in potential," Interface to Face 1, Center for Interface Science: Solar Electric Materials, a U.S. Department of Energy Frontier Research Center, Tucson, AZ, October 2010.
- Poster: "Electroabsorption spectroscopy for screening electrode functionalization in organic solar cells," Materials Research Society Fall Symposium D, December 2009.
- Talk: "Measuring electric fields in organic photovoltaics," University of Washington, 2009.
- Poster: "How do plastic solar cells work?" presented to the Seattle community leaders at Seattle Chamber Leadership Conference, October 2009.
- Poster: "How do plastic solar cells work?" presented to the general public, Shoreline SolarFest, Shoreline, WA, 2009.
- Poster: "Electrode functionalization in organic solar cells," University of Arizona, 2009.
- Poster: "Space charge limited photocurrents and mobility measurement in bulk heterojunction solar cells," Gordon Research Conference: Electronic Processes in Organic Materials, 2008.